UNIVERSITY OF OKLAHOMA

GRADUATE COLLEGE

ASSESSING THE UTILITY OF LOW-LEVEL BUOYANCY AND

COPTERSONDE MEASUREMENTS TO UNDERSTAND ATMOSPHERIC

BOUNDARY LAYER TRANSITIONS

A THESIS

SUBMITTED TO THE GRADUATE FACULTY

in partial fulfillment of the requirements for the

Degree of

MASTER OF SCIENCE IN METEOROLOGY

By

FRANCESCA M. LAPPIN
Norman, Oklahoma
2021

ASSESSING THE UTILITY OF LOW-LEVEL BUOYANCY AND
COPTERSONDE MEASUREMENTS TO UNDERSTAND ATMOSPHERIC
BOUNDARY LAYER TRANSITIONS

A THESIS APPROVED FOR THE
SCHOOL OF METEOROLOGY

BY THE COMMITTEE CONSISTING OF

Dr. Petra Klein (Chair)

Dr. Nusrat Yussouf

Dr. Scott Salesky

Acknowledgments

First and foremost, I would like the acknowledge that I have the privilege to view remotely-piloted aircraft systems (RPAS) as a tool for good. For a large population of people, RPASs are used for destruction. Of course, our purpose is purely for science, but this platform has historically been used for war. I would like to apologize to any person who experienced posttraumatic stress by the presence of our system. Our team will do everything we can to broadcast that our RPAS is only for scientific research.

For my personal acknowledgments, I would like to begin with my advisors and committee members. Thank you Dr. Phil Chilson for providing an endless breadth of research possibilities and giving me the freedom to explore my own interests. Your counsel allowed me to become a more independent and resilient scientist. I am entirely grateful to Dr. Petra Klein for supporting me through a turbulent transition and helping me mold my thesis. To my other committee members, Dr. Nusrat Yussouf and Dr. Scott Salesky, thank you for the perspective and contributions to my research. I would also like to thank Dr. Liz Pillar-Little who has been a constant supporter and advisor in life and research.

I would like to thank the LAPSE-RATE and Flux-Capacitor teams for collecting the data used in my thesis. Thank you, Brian Greene and Tyler Bell for not only processing the data but helping me process the chaos of the past two years. Brian, I might not have joined CASS without you and I certainly would not have survived without you. I also want to thank Tony Segales for engineering an amazing RPAS.

I would not be here today if it were not for the unconditional love from my friends and family. Every day I wear a piece of jewelry given to me by either my mother, sister, or aunt so that I can pull on the immense wisdom, strength, and bravery they emanate. To my mom, thank you for always bringing sunshine into my view, even when clouds hang low. To Anna Wanless and Lauren Pounds, you have been there every moment of my master's to hold me up and make me laugh. You are some of the

most inspiring scientists I have had the pleasure to know. To every other friend and family member, I appreciate you beyond words.

Table of Contents

5 Conclusions and Future Work   **62**

Reference List   **67**

Appendix   **78**

List Of Tables

List Of Figures

Abstract

Advancements in remotely piloted aircraft systems (RPAS) introduced a new way to observe the atmospheric boundary layer (ABL). Adequate sampling of the lower atmosphere is key to improving numerical weather models and understanding fine-scale processes. The ABL's sensitivity to changes in surface fluxes leads to rapid changes in thermodynamic variables. This study proposes using low-level buoyancy to characterize ABL transitions. Previously, buoyancy has been used as a bulk parameter to quantify stability. Higher-resolution data from RPASs highlight buoyancy fluctuations. RPAS profiles from two field campaigns are used to assess the evolution of buoyancy in convective and stable boundary layers. Data from these campaigns included challenging events to forecast accurately, such as convective initiation, a low-level jet, and katabatic flows. Results show that the ABL depth (ABLD) determined by the minimum in vertical buoyancy gradient agrees well with proven ABLD metrics, such as potential temperature gradient maxima. Moreover, in the cases presented, low-level buoyancy rapidly increases prior to convective initiation and rapidly decreases prior to the onset of a low-level jet. This study expounds on the utility of buoyancy in the ABL and contextualizes its use in comparison to Richardson number profiles.

Additionally, RPAS profiles are reviewed as an operational way to aid the forecasting of aviation weather. The concept of operations is described. Based on conversations with partners in the aviation community, a visualization of the RPAS data was designed to deliver the most desirable information. Restrictions on field campaigns caused by the COVID19 pandemic impeded the goal of regular profiling at a nearby airport. Nevertheless, a handful of scenarios are assessed from the perspective of a pilot. Finally, a discussion is provided on the complications of flying an RPAS at an active airport.

Chapter 1

Introduction

1.1   Atmospheric Boundary Layer

The atmospheric boundary layer (ABL) is strongly influenced by kinematic and thermodynamic interactions with the Earth's surface. It is sensitive to changes in radiation, low-level moisture, and heat fluxes. The ABL functions as a conduit for moisture and warm air to be transported vertically. As a consequence, the ABL depth (ABLD) and the ABL stability fluctuate in time and space (Lenschow et al., 1979; Stull, 1988). Turbulent structures drive thermal and moisture fluxes in attempts to equilibrate the ABL (Ohya et al., 1997). The numerous scales of motion present in the ABL often cause inhomogeneity. In turn, it becomes difficult to fully represent these processes, irrespective of their importance. This is especially true in the stable boundary layer (SBL) where turbulence is often intermittent and poorly simulated by numerical weather models (Sun et al., 2015). The multifaceted interaction between turbulence and the ABL is as enigmatic as it is crucial to understanding atmospheric processes.

The ABL is at the intersection of nearly all meteorological phenomena. As the interface between the surface and the lowest level of the atmosphere, the terrain can strongly influence ABL flows. For example, valley flows are comprised of katabatic (downslope) overnight and anabatic (upslope) winds during the day. Katabatic winds are driven by the cool, negatively buoyant air descending the valley walls. They often lead to persistent fogs (Chachere and Pu, 2016) and trapped pollution within the valley

(Whiteman and McKee, 1978; Pal et al., 2014). Impacts of this spill into public health as aerosols trapped in the SBL can trigger positive feedback mechanisms of severe pollution events (Li et al., 2017). Knowing the cold pool characteristics can help with predicting when the winds will shift to anabatic and increase mixing (Silcox et al., 2012). Proper forecasting for this has impacts spanning public health, transportation, and aviation.

Similarly, low-level jets (LLJ) are an ABL occurrence that impacts the public but are often misrepresented in models. The Great Plains LLJ is a warm-season, nocturnal wind maxima occurring below 1 km (Bonner, 1968). LLJs commonly transport pollutants and moisture (Stensrud, 1996; Hu et al., 2013; Sullivan et al., 2017). The mechanisms which drive the Great Plains LLJ stem from the sensitivity of the ABL to surface properties (Mccorcle, 1988; Fedorovich et al., 2017; Gebauer et al., 2017). As in the case of convective allowing models, ABL parameterizations have a large impact on simulated jets (Mirocha et al., 2016). LLJs foster the development of nocturnal storms by advecting warm, moist air from the south and supplying ascent near the jet exit and entrance regions (Bonner, 1966; Maddox, 1983; Astling et al., 1985; Trier and Parsons, 1993). As a result, the Great Plains receives more nocturnal rainfall during the summer months (Higgins et al., 1997). Models struggle to consistently represent the jets well, as the jet arrives too early and is slower than observations (Storm et al., 2009; Smith et al., 2019). Accurate simulations of cyclonic jet position and speed can significantly impact the forecast skill for precipitation (Squitieri and Gallus, 2016). The assimilation of radiosondes shows improvement to the simulation of LLJ strength over South America (Herdies et al., 2007; Skabar and Nicolini, 2009). Gathering data in the ABL increases representation whether it is based on improving parameterizations or through assimilation.

Lastly, thunderstorms have obvious societal impacts ranging from public safety to economic loss. The timing and exact location of convective initiation (CI) is a persistent issue in thunderstorm forecasting. Convective allowing models have greatly improved over the years, but CI is still a hindrance for successful forecasts. CI is thought to be highly dependent on environmental heterogeneities within the ABL (Frye and Mote, 2010; Rochetin et al., 2017). Nevertheless, it has proven difficult to observe the pre-storm environments adequately enough to diagnose thermodynamic differences. As a result, the majority of CI studies to investigate ABL processes utilize numerical weather models instead of observations (Kang and Bryan, 2011; Ryu et al., 2016; Chen et al., 2020). Where observational studies exist, the resolution of ABL observations has been insufficient to present clear results. While many field campaigns have made efforts to resolve the lack of ABL observations in convection studies, many questions leading up to CI remain (Browning et al., 2007; Rasmussen, 2015; Frew et al., 2020).

1.1.1 Buoyancy

Each of these processes, LLJs, katabatic flows, and CI are important weather events with significant societal impacts. However, a number of open questions remain regarding their formation and evolution. Here, we propose buoyancy as a process to help advance our knowledge of ABL phenomena. Buoyancy is a fundamental force in fluids caused by density differences that can drive vertical acceleration. Buoyancy has been used in attempts to forecast severe weather and is the basis for convective parameters like convective available potential energy (CAPE) and convective inhibition (CIN). CAPE is positive buoyancy integrated between the level of free convection and the equilibrium level, which may not always exist in every environment. In contrast, CIN is the culmination of negative buoyancy which suppresses thermal lift. Since CAPE is a bulk parameter, the most substantial contribution comes from the middle troposphere.

Climatologically, CAPE has correlated directly with storm intensity (Zhang and Klein, 2010) but has little short-term prognostic value (Ziegler and Rasmussen, 1998). CAPE and CIN lack the small-scale, near-surface effects needed to understand CI. As a result, mean radiosonde derived values of CAPE and CIN do not significantly differ between deep convection and fair weather days (Zhang and Klein, 2010). Yet, in the same study, average low-level (< 5 km) buoyancy does significantly differ. Moreover, single-level, simulated buoyancy values rapidly intensify, overcoming entrainment dilution prior to CI (Houston and Niyogi, 2007; Trier et al., 2014). Buoyancy is also used to quantify cold pool strength. Simulations indicate that an ample cold pool is key to long-lasting quasi-linear convective systems (Weisman and Rotunno, 2004).

Buoyant parcels rise from the warm surface and convectively mix the ABL. This process is the foundation behind most gradient-based ABLD methods. The ABLD is a key component of boundary layer parameterization and marks its evolution. Therefore, having accurate estimations of the ABLD is crucial for weather prediction. Nevertheless, many of the current methods lead to the ABLD having errors of 200 m (Anurose and Subrahamanyam, 2015). There are numerous ways to determine the ABLD, many of which are described and tested in Dai et al. (2014) and Dang et al. (2019). Notably, potential temperature proved to be a highly accurate method of estimating ABLD with vertical data resolution less than 20 m (Dai et al., 2014). Similarly, sharp gradients in humidity have been used to determine the ABLD for both stable and convective boundary layers when using lidar data (Hennemuth and Lammert, 2006). Dang et al. (2019) also evaluated different measurement systems to determine ABLD, which did not include RPAS, and determined lidar-based profiles would benefit NWP. A common thread throughout these studies is that there is no perfect determination for ABLD, nor is there a perfect platform.

4

Another phenomenon which could benefit from analysis using buoyancy is the LLJ. After decades of investigating the Great Plains LLJ, the generation and modulating mechanisms can be boiled down to a combination of processes. First, the cessation of daytime turbulence and frictional drag trigger inertial oscillations, which is commonly referenced in literature as the Blackadar mechanism (Blackadar, 1957a). Although, it does not explain how the LLJ can become supergeostrophic nor the frequency maximum over the Great Plains. Holton (1967) suggests that the downward slope of the Rocky Mountains causes differential heating and thermal forcing to increase southerly wind speeds. Shapiro and Fedorovich (2009) combined these theories to derive an inertial-gravity mechanism to explain the impacts of slope angle, stratification, and initial surface buoyancy. The analytical solutions completed in Shapiro et al. (2016) support the theory that the Blackadar and Holton mechanisms work in tandem to create LLJs consistent with observations. Shapiro et al. (2016) found that the larger maximum buoyancy leads to increased maximum jet speed, while changes to minimum buoyancy were less impactful. Using direct numerical simulations, Fedorovich et al. (2017) found that daytime buoyancy amplifies the inertial oscillation, therefore, strengthening the southerly jet. Conversely, large positive buoyancy impedes the initiation of northerly LLJs by creating an opposing force to the flow; such that a buoyancy maximum of zero or strongly negative buoyancy minimum is beneficial to the northerly LLJs (Gebauer et al., 2017). The LLJ's dependence on surface buoyancy is supported through many numerical studies, yet there are few studies looking at the observed evolution of buoyancy.

1.1.2 Richardson Number

Another classically used variable to interpret ABL processes is the Richardson number (Ri), which quantifies the balance between buoyantly induced or suppressed and

mechanically driven turbulence. Since the wind shear is positive definite, the sign of Ri is determined by thermal stability per Eq. 2.2. By convention, the negative sign is dropped preceding the buoyancy induced turbulence term, such that positive Ri corresponds to statically stable conditions. While buoyancy is a key component, Ri uses Brunt-Väisälä frequency squared or the buoyant frequency, rather than a parcel buoyancy definition as in Eq. 2.1. Theory and empirical results indicate there is a critical Ri_c where turbulence begins to decay (Rohr et al., 1988; Ohya et al., 2008). Similarly, there is a turbulence termination value Ri_T where turbulence ceases and flow becomes laminar. The values for each are not without disputation, but the generally accepted values are $Ri_c = 0.25$ and $Ri_T = 1$ (Stull, 1988). The altitude at which Ri_c is surpassed is also commonly used to determine ABLD (Vogelezang and Holtslag, 1996). In ABL research, Ri is often used to quantify the turbulent regime and stability, because it is sensitive to kinematic and thermodynamic changes. Buoyancy acts to generate or suppress turbulence in the form of turbulence kinetic energy (TKE). There is some correlation to increases in TKE when Ri goes below a critical level in downslope flow (Monti et al., 2002) and LLJs (Banta et al., 2003; Ohya et al., 2008). However, Sun et al. (2012) found that the relationship between Ri and TKE is dependent on the turbulence regime. LLJs are controlled by bulk shear, which reduces the thermal stratification through mixing driven by shear instability. As a result, Ri is reduced but not necessarily TKE.

Throughout many early turbulence field campaigns, tall masts collected data to calculate Ri (Lettau and Davidson, 1957). Frequently, Ri calculated below 50 m is used to describe the entire ABL due to platform constraints (Kondo et al., 1978; Mohan and Siddiqui, 1998). The ABL is rarely vertically homogenous, especially not in the SBL, so layer-specific information is lost. Further along, radiosondes, tethersondes, and remote sensors such as radars and lidars were used to calculate Ri profiles (Emmanuel,

6

1973; Poulos and Burns, 2003), but a variety of smoothing techniques must be applied to process the high-frequency data (Balsley et al., 2006; Chan, 2008; Dai et al., 2014). Since buoyancy and wind shear are two drivers to alter the ABL, it seems logical that Ri profiles would help conceptualize transitions in the ABL.

1.1.3 ABL Data Gap

In the past, it has proven difficult to collect adequate spatially and temporally resolved measurements within the ABL, resulting in a "data gap". Since the National Research Council (2009) called for more vertical measurements in the ABL, there have been technological advancements to address the gap. Remote sensors such as microwave radiometers, lidars, and scatterometers can continuously measure the lower atmosphere. The ongoing development of scanning strategies has widened the capabilities of sampling (Calhoun et al., 2006; Krishnamurthy et al., 2011; Wildmann et al., 2019). Measurements that were typically restricted to ground-based systems have expanded in conjuncture. Moreover, these remote sensing platforms are more mobile and gather a wider range of data than single point tower data. Assimilating these data have been shown to improve short-term forecasts (Coniglio et al., 2019; Hu et al., 2019; Lewis et al., 2020). Campaigns also increase opportunities for model validation (Chan and Leach, 2007; Wagner et al., 2019; Smith et al., 2019). All of which highlight the need for increased measurements in the ABL to improve collaboration between models and measurements.

It is crucial to point out that field campaigns are unique. Often, the terrain is complex and the results are not generalizable to all regions. There is also a logistical restraint to continually gather the data needed to improve models. These instruments are expensive and typically need to be used in tandem to get a complete sample. As with every system, there are drawbacks. Most remote sensors are mobile but not

nimble, which limits the environments they can sample. For example, pre-convective environments change rapidly, and instruments need to relocate quickly to gain targeted observations. Another tool more commonly used to capture ABL measurements is the radiosonde. Typically they are released twice daily across the United States. Their upper-air measurement aid greatly in seeing synoptic patterns throughout the troposphere. Unfortunately, radiosondes are only released frequently enough to capture mesoscale changes during field experiments. The spatial and temporal frequency of radiosonde release is inadequate for convective allowing models. Of equal importance, their spatial resolution through the ABL is too coarse for thorough characterization. While there are avenues to shrink the data gap, we still lack an infrastructure to address this on a broader scale.

1.2   Remotely Piloted Aircraft Systems

Remotely piloted aircraft systems (RPAS), also referred to as uncrewed aircraft systems (UAS) or vehicles (UAV), have flown since World War 1 (Desmond, 2018), but did not grow in popularity until 2006 when they were allowed into civilian airspace. Increasing interest in RPAS across many sectors has accelerated improvements in quality, cost, and availability of RPAS technology (Reuder et al., 2009; Elston et al., 2015; Villa et al., 2016). In turn, RPAS became more customizable, and their utility broadened. Therefore, their role in scientific research came naturally.

The benefits of utilizing RPAS in atmospheric sciences have been demonstrated across many situations. Small RPAS have the ability to take measurements in remote or hazardous environments such as in Antarctica (Jonassen et al., 2015), mountainous terrain (Mayer et al., 2012), hurricanes (Cione et al., 2016), and near supercells (Elston et al., 2011; Frew et al., 2020). Aided by the ability to deploy quickly, they

are well suited for rapidly changing environments. The reusability of RPAS create a cost-efficient method to repeatedly sample evolving environments. Most weather sensing RPAS fall into the fixed-wing or rotary-wing category. The best choice is often dependent on the desired observations. Fixed-wing RPASs offer transects of the atmosphere allowing a larger area to be sampled. However, the vertical resolution of data is decreased by the inability to do fixed location profiles. Meanwhile, rotary-wing RPAS are typically lighter and require less space to deploy. Profiles can be completed in a fixed location, which reduces errors that would be introduced in a heterogeneous environment. Although rotary-wing RPAS cannot travel as far as fixed-wing RPAS, profiles can be completed frequently so long as batteries can be readily replaced. Given these various capabilities, data from RPAS can capture flow evolutions and ABL transitions (Cassano, 2014; Bonin et al., 2013). Balsley et al. (2018) uses a fixed-wing RPAS in a helical ascent and descent to gather Ri profiles amongst other turbulent parameters. The nature of the slant-path flight strategy causes some inflated wind shear measurements, reducing Ri. Close attention to sensor placement and calibration reduce systematic errors (Jacob et al., 2018; Greene et al., 2019). Confidence in these data is supported by Bell et al. (2020), finding measurements from RPAS, radiosondes, and remote sensors all agree well with each other. This study also discusses the functionality of each platform. Moreover, the data collected has continually shown to improve model accuracy and reduce forecast bias (Jonassen et al., 2012; Ágústsson et al., 2014; Flagg et al., 2018; Jensen et al., 2021). Complementing remote sensing platforms, RPAS offer another option to address the data gap.

While RPASs allow for more adaptive sampling, there are many federal regulations and air restrictions governing their use. The Federal Aviation Administration (FAA) has recently instituted new programs to facilitate the expansion of RPAS for commercial use, such as the Low Altitude Authorization and Notification Capability

(LAANC). This has increased the number of approved flight waivers. Trends suggest that RPAS used in atmospheric research will become more common based on a few factors. The combination of greater availability of weather sensing RPAS and reduced obstacles to attain flight permissions will aid accessibility. The confidence shown in the data collection and usefulness in data assimilation will prove its place as a reliable observation platform. RPASs stand as an affordable, portable option that can be used in tandem with remote sensing platforms for a more complete sampling of the ABL.

Novel platforms such as RPAS deliver unprecedented data sets. While some people view rotary-wing RPAS as an alternative to radiosondes, using only radiosonde-based methods on RPAS data would encumber the possibilities accompanied by this new data set. Alongside the evolution of observation platforms, there must also be an advancement in the methods. In this study, two traditional ABL variables used to quantity stability (buoyancy and Ri) will be analyzed in unconventional ways. The time-height evolution of buoyancy under different ABL phenomena will be analyzed. Using the high spatiotemporal resolution data from rotary-wing RPAS, ABL features and transitions will be dissected. The following analysis will include three cases: the diurnal ABL cycle under the influences of an LLJ, pre-convective conditions at two locations within an elevated valley, and katabatic flow impacts on the morning transition. Profiles of Ri will be used to look into the LLJ and katabatic flow cases. A critical analysis of each method will be done to determine if either variable is useful in examining ABL transitions. The goal is to expound on the unique advantages gained by viewing ABL processes through the lens of buoyancy and Ri.

Chapter 2

Data & Methods

2.1 Field Campaigns

Here we consider examples of data collected using RPAS and radiosondes during two different field campaigns. Both campaigns aimed to demonstrate the usefulness of RPAS for examining various atmospheric phenomena. Flux-Capacitor sampled the diurnal boundary layer cycle as well as a common southern plains occurrence, the LLJ. The Lower Atmospheric Process Studies at Elevation—a Remotely Piloted Aircraft Team Experiment (LAPSE-RATE) campaign was uniquely located at high-altitude with orographically driven circulations and different land surfaces. We will use these data to evaluate the utility of low-level buoyancy in diverse environments. All flights completed during both campaigns were conducted under FAA certificates of authorization (COA) and overseen by FAA licensed pilots, who were embedded with the research teams. A complete description for each campaign follows.

2.1.1 Flux-Capacitor

The Flux-Capacitor field campaign took place as a test of the 3D Mesonet concept in which a subset of Oklahoma Mesonet stations would include an RPAS capable of regularly profiling the lower troposphere (Chilson et al., 2019). The campaign tested the feasibility of continuous flights to observe the ABL transition over a 24-h period.

Flights began at 1501 UTC (1001 LST) 05 October 2018, taking off every 30-min, and with the last flight at 1430 UTC (0930 LST) on 06 October 2018. A flight to 1 km above ground level (AGL) takes roughly 12-min. This campaign sampled the ABL throughout its diurnal cycle. The typical cycle was modified by a southerly LLJ. The flight ceiling for Flux-Capacitor was based on line of sight operations up to 1,200 m. Due to strong winds, the RPAS was unable to reach maximum altitude. Flights took place 28 km southwest of Norman, OK, USA at the Kessler Atmospheric and Ecological Field Station (KAEFS), which is co-located with the Oklahoma Mesonet's Washington station (WASH). Additionally, a radiosonde was released approximately every 3 hours, for a total of 10 soundings. Radiosondes served as a means to validate measurements from RPAS profiles. A suite of remote sensors within the Collaborative Lower-Atmospheric Mobile Profiling System (CLAMPS) also supplemented the dataset.

2.1.2 LAPSE-RATE

Figure 2.1: The San Luis Valley with markers at each CASS deployment site. A) K04V, B) MOFF, C) SAGF (courtesy © Google Earth 2021)

LAPSE-RATE took place in San Luis Valley, Colorado (38° N, 106° W) from 14–20 July 2018 following the International Society for Atmospheric Research using Remotely-piloted Aircraft (ISARRA) conference (de Boer et al., 2020b). Ten teams gathered to collect atmospheric measurements using RPASs for three targeted missions: convective initiation (CI), drainage flows, and boundary layer transition. Teams distributed across the valley regularly collected synchronized, vertical profiles of the atmospheric state up to 914 m above ground level with rotary-wing RPASs. Additional data were collected using fixed-wing RPAS, radiosondes, and ground-based remote sensors. This study will focus on the stations by the University of Oklahoma's Center for Autonomous Sensing and Sampling (CASS). The same RPASs used in LAPSE-RATE were used in Flux-Capacitor. CASS had three profiling stations, one at Moffat School (MOFF), Saguache Airport (K04V), and Saguache Farms (SAGF). Seen in Fig. 2.1, all CASS sites were

located in the northern section of the valley. The MOFF site was located within the valley basin. The K04V site was located where the Saguache Canyon spills into the San Luis Valley. K04V was flanked by mountains to its north and southwest. SAGF was 10 km southeast of K04V in an irrigated alfalfa field. During ABL transitions, flights were completed at 15 min intervals. Otherwise, the flight frequency was 30 min. Flight cadence at each site was not always synchronous due to weather conditions.

This campaign was unique in location and execution. The San Luis Valley has an average elevation of 2,300 m and peaks at 4,000 m above sea level. The valley was arid but contains irrigated cropland creating gradients in temperature and moisture from differing land uses. There was orographic lift, which led to convection commonly occurring overtop the mountains. Furthermore, mountain-valley circulations affected ABL transitions and air quality. Teams were able to partially sample the valley, which is nearly the size of Connecticut, by completing over 1,200 flights, using 34 different platforms (de Boer et al., 2020a; Pillar-Little et al., 2021).

Conditions within the valley were ideal for RPAS flights and observing mesoscale to microscale flow features. de Boer et al. (2020a) provided a description of the weather conditions. In summary, due to limited moisture, temperature and humidity have a strong diurnal cycle that drives flow features. In the afternoon when the ABL is approximately dry-adiabatic, winds are gustier and occasionally enhanced by outflow from mountain convection. Both observations and simulations from Pinto et al. (2021) indicate a diurnal drainage flow pattern at K04V every day. As a result, a cold pool forms within the valley basin. While these conditions were a daily trend, the week of LAPSE-RATE had a variety of conditions to sample. The first 2 days of structured flights (15-16 July 2018) were selected to study CI. Both days had moisture advected from the Pacific Ocean with a passing cold front. The cold front was weak and lack of wind shear promoted isolated convection. After the 17th, a high-pressure system with

mid-level drying diminished all convective potential. Thus, the focus was turned to morning ABL transitions. The 19th was focused on capturing cold-air drainage flow, hence flights began shortly before sunrise. A gamut of atmospheric phenomena was captured during LAPSE-RATE, but this study will focus on CI and cold-air drainage.

2.2 Observation Platforms

During the LAPSE-RATE campaign, there were numerous RPASs collecting data in addition to remote sensing platforms and ground station observers. All data obtained during LAPSE-RATE can be found at https://zenodo.org/communities/lapse-rate/. Flux-Capacitor utilized the CopterSonde, radiosondes, CLAMPS, and surface observations. Both campaigns used the same three CopterSondes to collect all data. This study will primarily use data from the CopterSonde and radiosondes. The two platforms share similarities in quantities and dimensions sampled. Nonetheless, there are stark differences in abilities. Radiosondes are capable of sampling a much taller column, while the CopterSonde's flight ceiling is limited greatly by regulation, technology, and atmospheric conditions. Radiosondes are not true Eulerian platforms; they are advected with the flow, adding quasi-Lagrangian impacts. As a result, observations are coming from downwind of the release site, especially for Flux-Capacitor since there was a strong LLJ. The CopterSonde conducts fixed location profiles delivering true local vertical gradients. Moreover, the per-profile cost of a radiosonde release is much higher than a CopterSonde profile, restricting the temporal resolution of radiosonde releases. Nevertheless, the long-established confidence in radiosondes makes them a validation tool for measurements from the CopterSonde. The description for each of these platforms follows.

2.2.1   CopterSonde

Parameter	Range	System accuracy
Temperature	-20-40 °C	0.5 °C
Relative humidity	0-100%	2%
Pressure	10-1200 hPa	1.5 hPa
Wind speed	0-25 m s^{-1}	0.6 m s^{-1}
Wind direction	0-360°	4°

Table 2.1: CopterSonde measurement specifications and accuracies compared against measurements from Vaisala RS92-SGP based on Bell et al. (2020)

The RPAS utilized in both field campaigns is the CopterSonde 2. This is a rotary-wing quadcopter designed and manufactured by the CASS at the University of Oklahoma. The CopterSonde contains three temperature sensors (iMet-XF glass bead thermistors) and three relative humidity sensors (Innovative Sensor Technology HYT 271). The measurement range of each sensor comes from the manufacturer and the accuracies compared against values measured by the radiosondes are found in Table 2.1. All sensors are placed within the shell of the aircraft, protecting them from solar radiation and heat from the motor, which can impact the precision of the measurements (Greene et al., 2018, 2019). Built into the shell is an aspirated intake scoop that is designed to consistently draw air across the sensors and adapts to position the intake scoop into the wind. An algorithm using roll, pitch, and yaw details from the autopilot determines the wind speed and direction. Consequently, this improves measurement accuracy and eliminates the need for additional wind sensors (Segales et al., 2020; Greene et al., 2019). Pressure is determined by the MS561 pressure sensor within the autopilot. The sensor scoop was tested in the Oklahoma Climatological Survey

calibration laboratory. The linear bias for each sensor was calculated and applied to the post-processed CopterSonde data. Afterwards, if a temperature sensor had a bias > 0.5 °C its data were removed. Adjustments are built off of trials from previous campaigns such as Environmental Profiling and Initiation of Convection (EPIC; Koch et al. (2018) and 2018 Innovative Strategies for Observations in the Arctic Atmospheric Boundary Layer (ISOBAR; Kral et al. (2018)).

2.2.2 Radiosonde

Radiosondes have stood as the standard for atmospheric measurements for over 90 years and serve as a validation tool for many novel sensing platforms. The Vaisala RS92-SGP radiosonde is used for this study. Data from the radiosondes are initiated from ground station data. According to Vaisala technical data, there is a 0.5 °C uncertainty for temperature and 5% uncertainty for relative humidity. The measurement response time for both sensors is less than 0.5 s. Data are automatically post-processed using a proprietary method specific to Vaisala. Further information regarding the radiosondes used during LAPSE-RATE can be found in Bell et al. (2021).

Date	Time	# of flights	Δt (min)	Location	Mission
20180715	1326-1944	18	15	MOFF	CI
20180715	1400-1915	12	30	K04V	CI
20180719	1150-1700	24	15	MOFF	Drainage flow
20180719	1130-1700	22	30	SAGF	Drainage flow
20181005	1500-2335	18	30	KAEFS	LLJ
20181006	0000-1431	28	30	KAEFS	LLJ

Table 2.2: Summary of CopterSonde flights from Flux-Capacitor and LAPSE-RATE. Time in UTC. Δt (min) is the average time between takeoff

2.3 Methods

The CopterSonde allowed for controlled measurements taken at a prescribed frequency specified by the needs of each campaign. Table 2.2 describes flight strategies in both experiments. Abiding by FAA air regulations, the flight ceiling for Flux-Capacitor was 1,524 m (5,000 ft) AGL with line of sight operations required. Lights affixed to the RPAS allowed visibility into the night, but due to high winds, a majority of Flux-Capacitor flights did not reach the flight ceiling. As for LAPSE-RATE, flights were authorized up to 914 m (3,000 ft) AGL, which most flights reached.

Buoyancy (β) was calculated at each level using

$$\beta = g * \frac{T_{v,par} - T_{v,env}}{T_{v,env}} \tag{2.1}$$

such that the vertical resolution stays 3 m for Flux-Capacitor and 10 m for LAPSE-RATE. The parcel's virtual temperature ($T_{v,par}$) was calculated based on parcel theory with the lowest observed temperature and dew point used as the initial inputs. The temperature and relative humidity measured by the RPAS or radiosonde were used to calculate the virtual temperature which functions as the environmental temperature ($T_{v,env}$) while g is the acceleration due to gravity. Example profiles $T_{v,par}$, $T_{v,env}$, and β using CopterSonde data are provided in Fig. 2.2.

The gradient Richardson number (Ri) was calculated using

$$Ri = \frac{g}{\theta} * \frac{\frac{\partial \theta}{\partial z}}{(\frac{\partial u}{\partial z} + \frac{\partial v}{\partial z})^2} \tag{2.2}$$

Since the data were not heavily smoothed, vertical gradients applied to the wind components induced large variations in values. In attempts to constrain the Ri fluctuations, an array of smoothing techniques were tried. A full description of methods tested to

make the CopterSonde data more comparable to the radiosonde data is found in Appendix A. Ultimately, the best option came from running means of 100 m for u and v wind components, 20 m for potential temperature, and 5 m for the wind speed and potential temperature gradients. This method reduced root-mean-square error (RMSE) while preserving significant fluctuations.

CopterSonde data were post-processed before being included in this analysis. The thermistors and pressure sensors record data at 20 Hz and the humidity capacitor records data at 10 Hz. To unify the sampling rate of all sensors, all data were interpolated to a 10 Hz frequency. Subsequently, the offsets gained from calibrations were applied and data from the duplicate sensors were averaged together. The data were then averaged to 3 m bins for Flux-Capacitor and 10 m bins for LAPSE-RATE. Only the data collected in the ascending portion of the flight were used. Since the CopterSonde ascends slower than it descends, the sensor response time aligns better with ascent speed (3 ms^{-1}). An in-depth description of data processing for the LAPSE-RATE campaign can be found in Pillar-Little et al. (2021) and procedures were very similar for Flux-Capacitor data. The radiosonde data were vertically interpolated to mimic the sampling resolution of the CopterSonde of 3 m for Flux-Capcitor and 10 m for LAPSE-RATE. The summed buoyancy for the radiosondes was calculated up to the flight ceiling for the CopterSonde closest to release time. Since flight ceilings change based on flying conditions, this was done to make the results most comparable.

Various methods were used to determine the ABLD during Flux-Capacitor. To smooth over some individual spikes in the CopterSonde data, a 5-point (15 m) running mean was applied across the entire profile to derived quantities including, potential temperature, dew point temperature, mixing ratio, and buoyancy. This was not necessary for the radiosonde data since it was processed by Vaisala software then additionally

vertically interpolated. Further description of the methods for calculating ABLD can be found in Section 3.3.2.
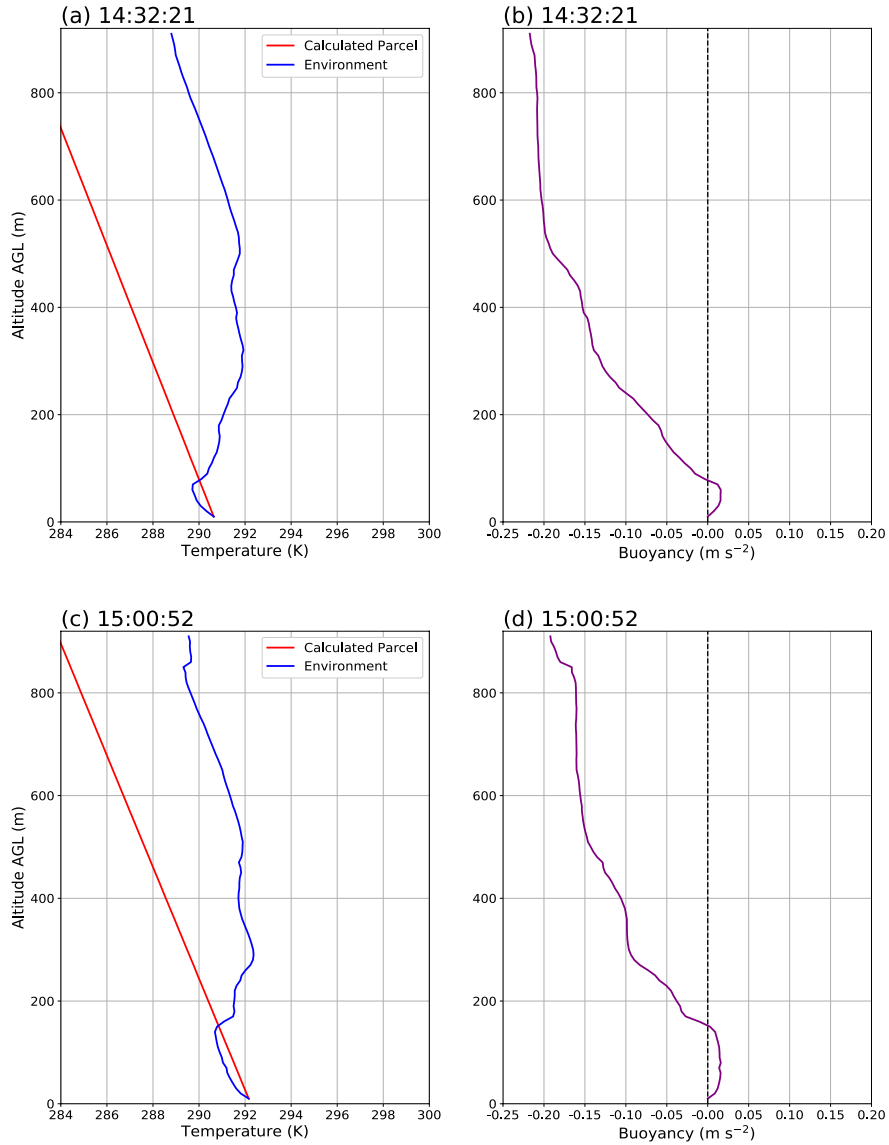
Figure 2.2: Temperature (K) and buoyancy (m s^{-2}) profiles from CopterSonde at MOFF on 19 July 2018. (a,c) Temperature observed from CopterSonde (blue) and dry adiabatically lifted parcel (red). (b,d) Calculated buoyancy profile (purple) with zero buoyancy line (dashed black).

Chapter 3

Fundamental RPAS Applications

3.1   Case Analysis

3.1.1   Low-Level Jet Evolution
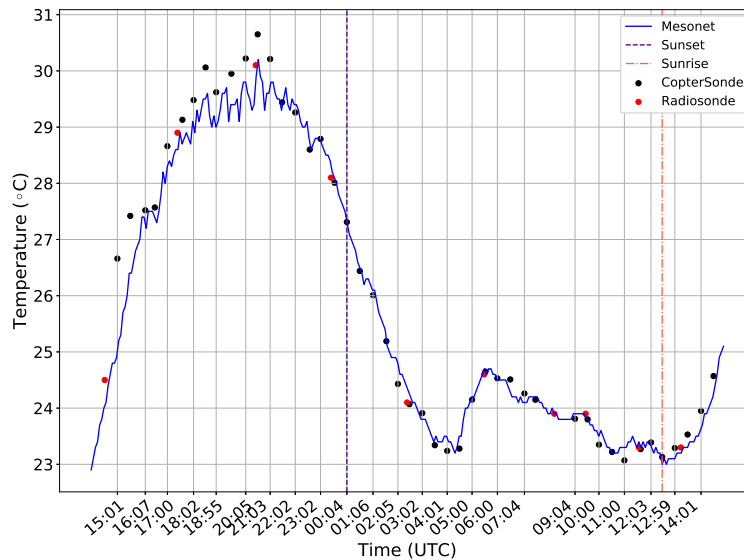
Figure 3.1: Time series of temperature (°C) measured at the lowest level from the Mesonet (9 m) (blue line), CopterSonde (6 m) (black dot), and radiosondes (7 m) (red dot) on 05-06 October 2018. Purple and orange vertical lines represent sunset and sunrise, respectively.

Figure 3.1 shows the temperature at the lowest measured elevation from both platforms, 6 m for CopterSonde and 7 m for radiosonde, in addition to the Oklahoma Mesonet's 9 m temperature observation. Given the thermistor response time of <2 s,

the CopterSonde has enough time to acclimate to the air temperature at 6 m. The radiosondes used in this field campaign take in the station measurements as a boundary condition, which explains the strong agreement between radiosondes and Mesonet data. Initially, the CopterSonde has approximately a 1°C warm bias at the lowest elevation. This is a consequence of the shell being heated by the sun during the site setup. Continuous aspiration over the sensors above the surface would reduce this effect at higher elevations. The recurrent flights afterwards prevented the CopterSonde from sitting in the direct sun long enough to heat up. Such that, the warm bias reduces below 0.5°C after 1607 UTC. Keeping the instrument in the shade until takeoff is now the standard to mitigate the overheating effect. Therefore, there is confidence in the accuracy of temperature measurements, thus the initialization point for buoyancy profiles.
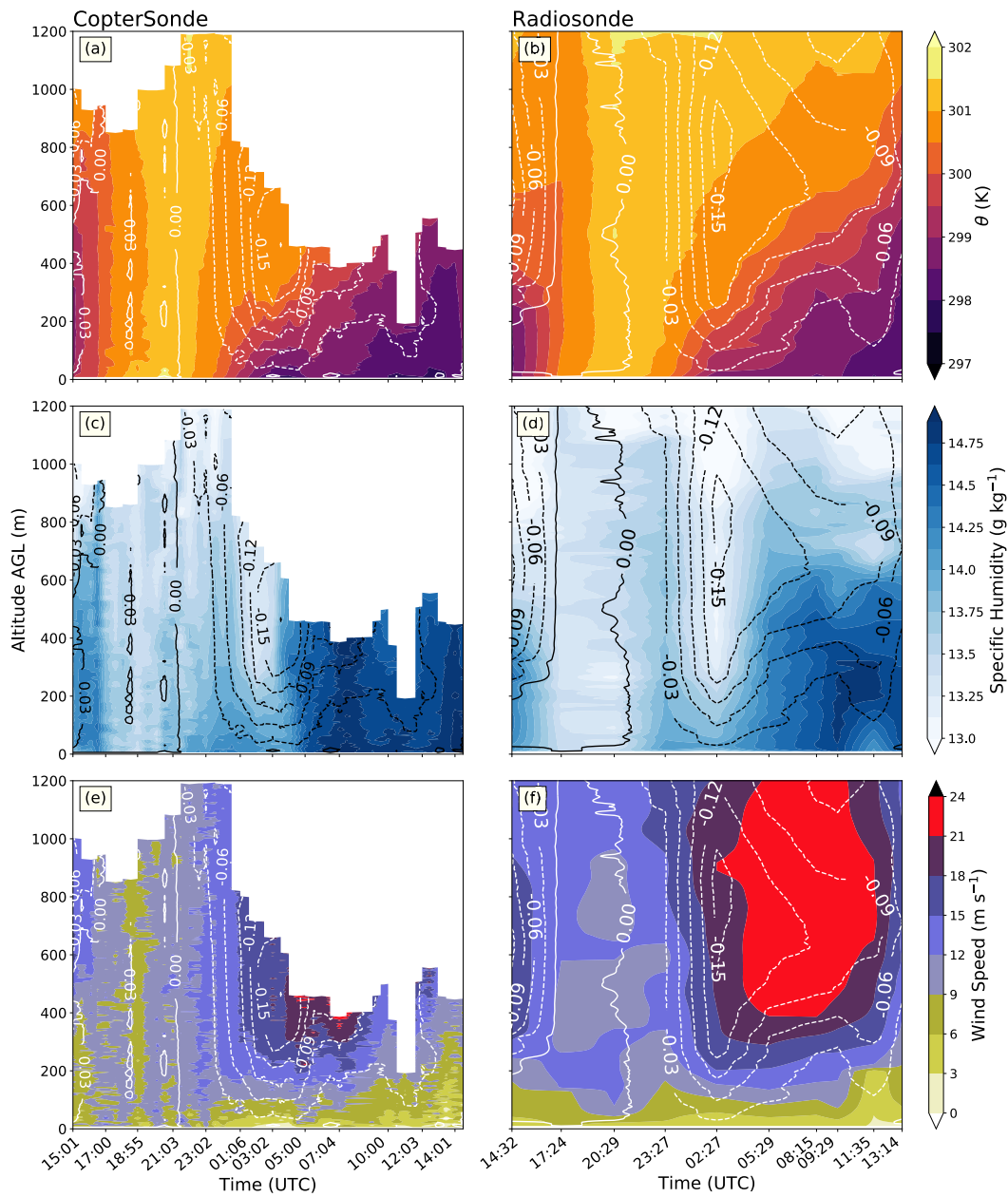
Figure 3.2: 05-06 October 2018 shaded contour fields of (a,b) potential temperature (K), (c,d) specific humidity (g kg $^{-1}$), and (e,f) wind speed (m s $^{-1}$) with buoyancy contours overlaid (m s $^{-2}$). Dashed(solid) contours are negative(positive). Left column (a,c,e) use CopterSonde data and right column (b,d,f) use radiosonde data.

Figure 3.3 shows the evolution of the vertical summation of buoyancy throughout time. Since buoyancy is dictated by temperature differences, diurnal changes in insolation give the graph a sinusoidal shape. This is seen in both platforms even though there is some variability. While not shown, the depth of the summation did not impact the overall shape, only the magnitude. Peak vertically summed buoyancy occurs at the same time as peak surface temperature (Fig. 3.1). As incoming solar radiation begins to decrease, buoyancy decreases (Fig. 3.3). Contrary to assumptions in Shapiro et al. (2016), the maximum buoyancy occurs about four hours before sunset. Upon the arrival of the LLJ, there is a rapid increase in buoyancy as a result of surface warming. Turbulent forces act to return the ABL to a neutral state. The SBL begins to erode before sunrise, thus allowing the environment to quickly become positively buoyant once daytime heating begins.
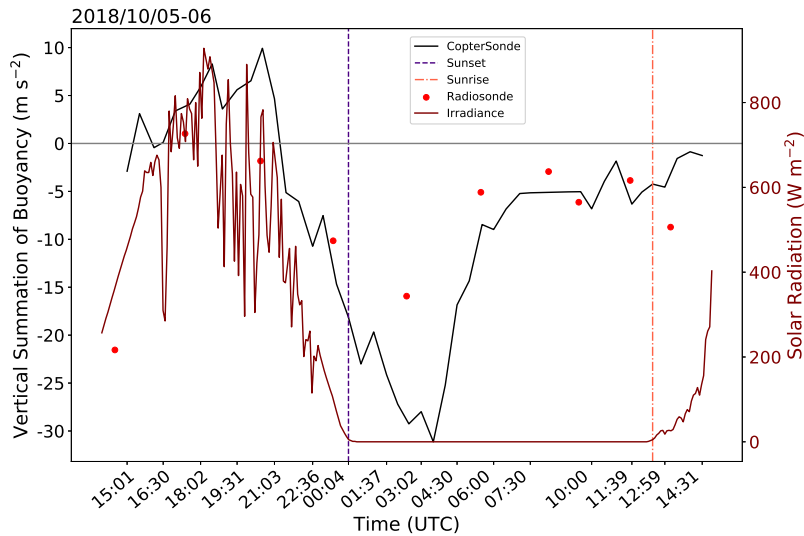
Figure 3.3: Time series of the vertically summation of buoyancy (m s^{-2}) on 05-06 October 2018. Black line is CopterSonde data, red dots are radiosonde data. Maroon line is the incoming solar radiation (W m^{-2}) measured by the WASH Mesonet. Purple and orange vertical lines represent sunset and sunrise, respectively

Looking at the LLJ through a different lens, Ri profiles are calculated with every flight and radiosonde release. The profiles of Ri from radiosonde data will be compared to that of CopterSonde data to test the feasibility of gathering Ri profiles from the CopterSonde. The overnight environment is high shear, but also thermally stratified. Under these circumstances, values of $0 < Ri < 1$ are expected below the jet and $Ri > 1$ are expected within the jet. A major drawback to this analysis comes from the proprietary pre-processing techniques applied to the radiosonde data. Since Ri is highly sensitive to the sampling rates and smoothing techniques, differences in data processing introduces inherent, incalculable errors (Balsley et al., 2006). With this in mind, deviations in Ri profiles from the two datasets are unavoidable. Nonetheless, the following analysis aims to recognize similarities, give critique, and supplement the LLJ analysis.
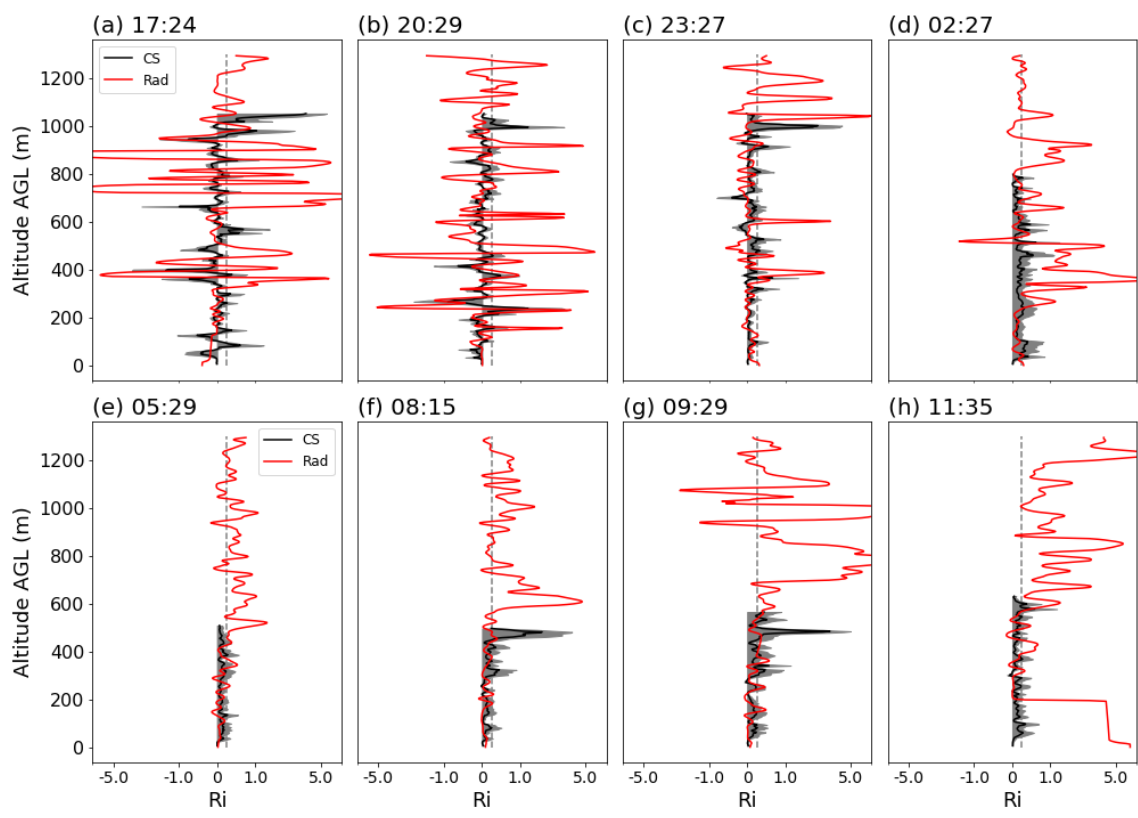
Figure 3.4: Ri from single radiosonde release (red) and 5 CopterSonde profile averaged profile (black) with gray shading as the standard deviation on 05-06 October 2018. Times listed are the time of radiosonde release (UTC) the CopterSonde profiles were averaged with that time as the center.

A temporal average of 5 CopterSonde profiles is performed centered around each radiosonde release time. Not only is the number of profiles condensed, but it also displays the spread over a roughly 2 h span. Figure 3.4 shows the Ri profiles from the temporally averaged CopterSonde flights and radiosonde releases. The gray shading represents a single standard deviation on each side of the mean CopterSonde profile. Except for a few instances, the error range is within a magnitude of the mean. The skewness is negative, as the 1-sigma range trends on the positive side. The profiles agree decently well with each other within the range of two hours. The largest inconsistencies

occur beneath the jet at the top of the profile (Fig. 3.4f, g). Each of these averages includes profiles from when the jet arrives and exits, adding spread to the wind shear profile. The largest deviations correspond to the time and area in which the ABL would be varying the most within a few hours.
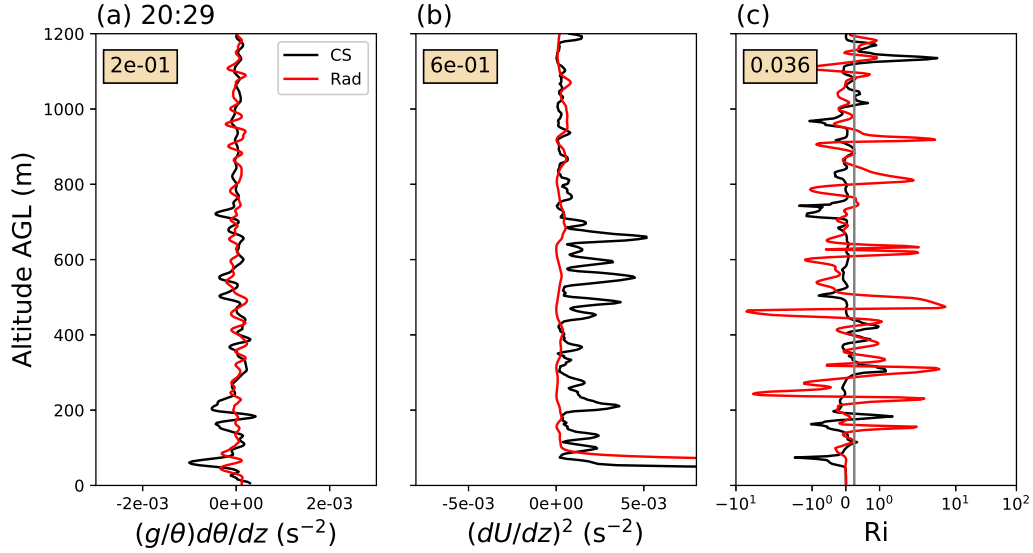
Figure 3.5: Ri and its components on 2029 UTC 05 October 2018 from CopterSonde (black) and radiosonde (red) data. (a) Brunt-Väisälä squared term (s^{-2}). (b) Squared vertical wind shear (s^{-2}). (c) Ri with height. The tan boxes indicate the RMSE between the CopterSonde and radiosonde values.

The initial difference between radiosonde and CopterSonde Ri values is stark but improves under less convective conditions, after 2327 UTC. The radiosonde Ri in a convective boundary layer (CBL) fluctuates more intensely than the CopterSonde data (Fig. 3.4a, b). Figure 3.5 shows the two gradient components of Ri and points out where the substantial difference lies. The radiosonde wind shear profile is nearly zero above 80 m (Fig. 3.5b), even though Fig. 3.2b shows some vertical speed shear, which causes the small fluctuations in buoyancy frequency to be grossly amplified. The overall

appearance of each platform's buoyancy frequency is very similar (Fig. 3.5a). Another instance occurs at 0227, Fig. 3.4d, from 300-500 m the average difference is an order of magnitude. The CopterSonde flight ceiling is around 800 m and measured   17 m s^{-1} wind speeds (Fig. 3.2e). Meanwhile, the 0227 UTC radiosonde release measures slightly stronger winds at   20 m s^{-1} (Fig. 3.2f). Since the radiosonde is not a true Eulerian tracer, it is advected with the flow. Being carried along with the mean flow rather than ascend right through it distorts the actual, vertical wind shear. Different locations introduce another detraction from a direct comparison of observation.

As expected, the evolution of Ri follows changes in the ABL. During the CBL, $|Ri| < 0.5$ and often negative due to instability (Fig. 3.4a-c). As the warmest part of the day approaches, Fig. 3.5b shows a prominent surface layer with strong wind shear within the lowest 50 m and a very well-mixed layer above. Within the mixed layer, Ri oscillates about 0 (Fig. 3.5). The evening transition causes a larger standard deviation with the CopterSonde profile but remains positive as the SBL forms. Below the LLJ, Ri is constrained by strong wind shear (Fig. 3.4e-h). Within the jet, shown by the radiosonde profile, the homogeneous wind speed allows Ri to surpass R_T and change rapidly (Fig. 3.4f-h). Looking at the CopterSonde data, the 3 CBL profiles (Fig. 3.4a-c) and the 5 SBL profiles (Fig. 3.4d-h) are similar to each other based on respective stability regime. There are times where the spikes are larger or there is more spread but broadly there are few unique features. Diagnosing the environment on Ri profiles alone seems ill-fitting, considering even the transition periods are nonspecific. The radiosondes offer a bit more nuance under the jet, aided by more data at jet height. Differences between radiosonde profiles illustrate the shift in dominating turbulent mechanism from buoyancy during the day and wind shear overnight (Fig. 3.4). In this case, Ri profiles offer some environmental description but an incomplete representation.

Foundationally, there can be no ideal comparison without the data being processed comparably. Nevertheless, Ri profiles from each data set share some similarities. Nearly all values are the logical sign and magnitude. During times of transition, the sign change is at roughly the same height. Although, the sensitivity of Ri makes it incredibly difficult to compare two data sets with different processing techniques. Vertical gradients of potential temperature and wind shear are often small and impacted by a range of potential errors which cause large fluctuations. Looking only at the Copter-Sonde Ri profiles, the errors appear to occlude some of the LLJ-induced structures. The buoyancy field offers more representation of vertical layers and transitions. In the context of an LLJ, the CopterSonde is more apt in representing fine-scale features using buoyancy than Ri.
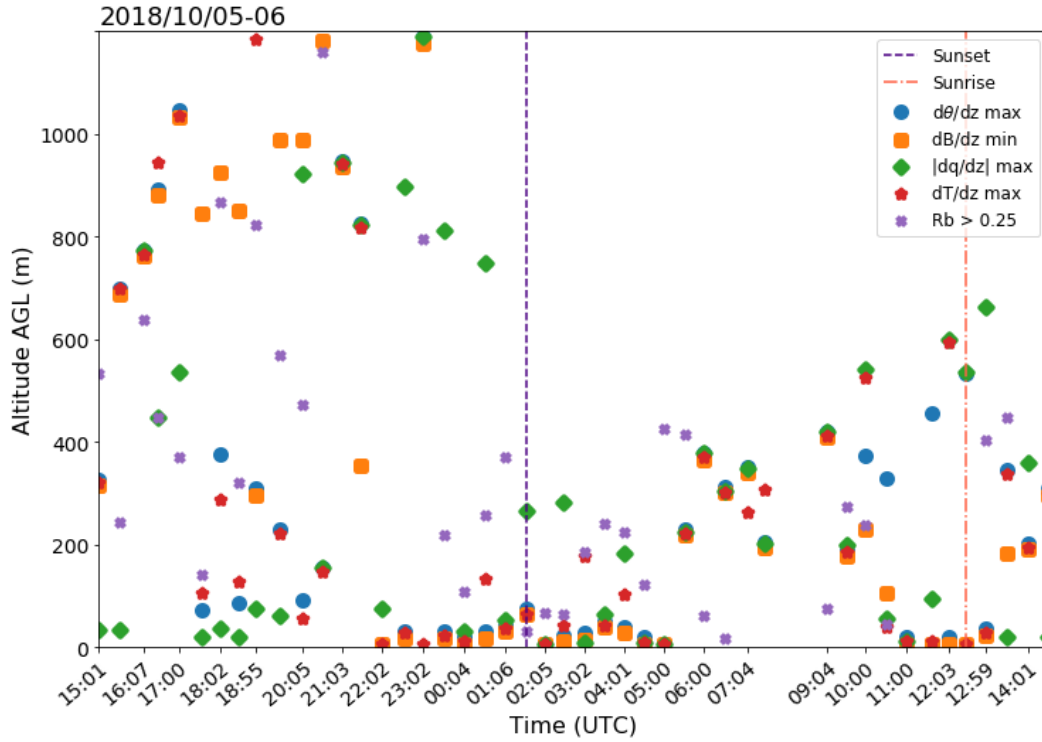
Figure 3.6: ABLD (m) determined by 5 different methods, maximum potential temperature gradient (blue circle), minimum buoyancy gradient (orange square), absolute maximum in specific humidity gradient (green diamond), maximum temperature gradient (red star), and $Rb > 0.25$ (purple x). Orange dashed line indicates time of sunrise. Purple dashed line indicated time of sunset.

3.1.2   ABL Depth

After the initial analysis seen in Fig. 3.2, it was observed that buoyancy is roughly constant with height in a CBL. This is as expected, since buoyancy is a driving force to homogenize the ABL. Therefore, a gradient-based method is proposed to find the ABLD from buoyancy profiles. There are numerous methods and variables used to find

the ABLD. These five ABLD methods are tested and compared using only Copter-Sonde data: maximum potential temperature gradient (Martucci et al., 2007), minimum buoyancy gradient, bulk Richardson number (Rb) > 0.25, absolute maximum in specific humidity gradient and maximum temperature gradient (Hennemuth and Lammert, 2006). Most agreement happens during the morning transition and evening transition. During this time, the full mixed layer is captured within the flight ceiling and a clear transition layer can be found (Fig. 3.6). The Rb method relies on the idea that nearly all turbulence is contained within the ABL, such that the height at which the critical Rb number is surpassed (Rb>0.25) indicates the top of the ABL. The Rb method appears to be the least successful in the CBL due to consistent underestimation. As discussed in the Appendix A, Rb profiles are highly dependent on the layer depth and values are too small when the layer depth from Dai et al. (2014) is used. The wind shear is highly variable which leads to noisy Rb profiles. Consequently, there are lulls in wind shear that trigger the ABLD somewhere within the mixed layer. Additionally, large wind shear values can lead to the ABLD not being found since Rb is so small. For these reasons, the Rb method could not reliably be used to test against the buoyancy gradient method. As for the other gradient methods, there are few distinct differences. Ultimately, the potential temperature gradient method is selected as the control method to compare against buoyancy.
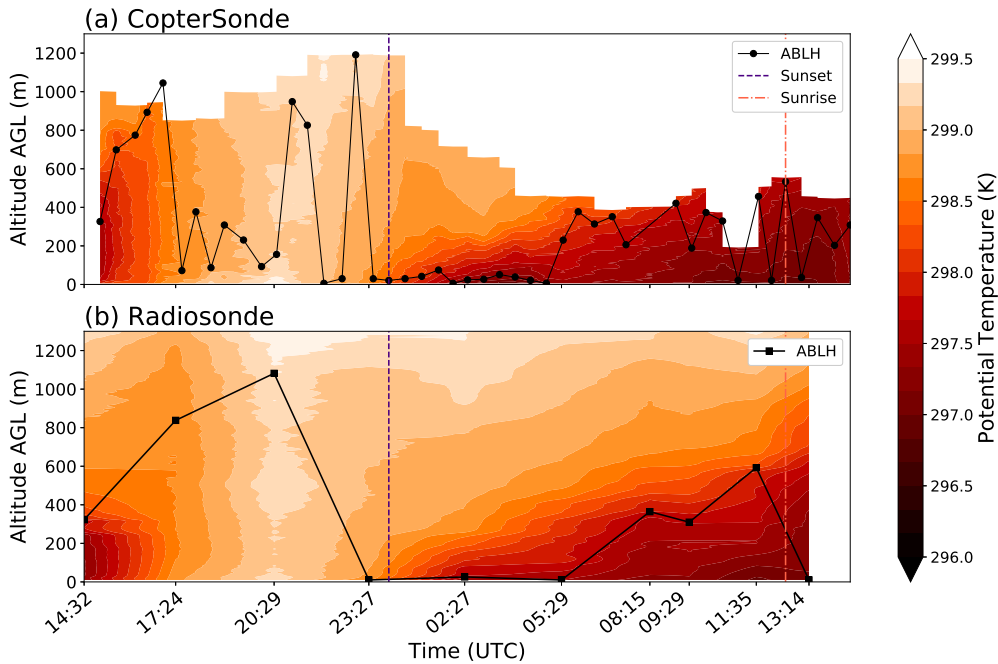
Figure 3.7: Potential temperature field (shaded contours) and black line indicating the ABLD determined by height of maximum potential temperature gradient on 05-06 October 2018. (a) each circle indicates the height determined by an individual flight. (b) each square indicates the height determined by an individual radiosonde.

The potential temperature method, radiosonde derived heights (Fig. 3.7b) do not change as rapidly as those derived from the CopterSonde data (Fig. 3.7a). Moreover, the potential temperature method ABLD from the CopterSonde data are lower from 1724-2300 UTC compared to radiosonde-derived heights. The dropoff in ABLD occurs once the mixed layer extends past the flight ceiling. Without a strong transition above the ABL, the potential temperature method erroneously finds where the surface layer transitions to the mixed layer. The CopterSonde is more likely to find these sharp gradients near the surface because of the increased data resolution at lower levels. The heights derived from the CopterSonde are deterred by the flight ceiling, which leads to

33

a low bias in ABLD. An aside, some heights appear to surpass the provided data, this is a smoothing artifact from plotting.
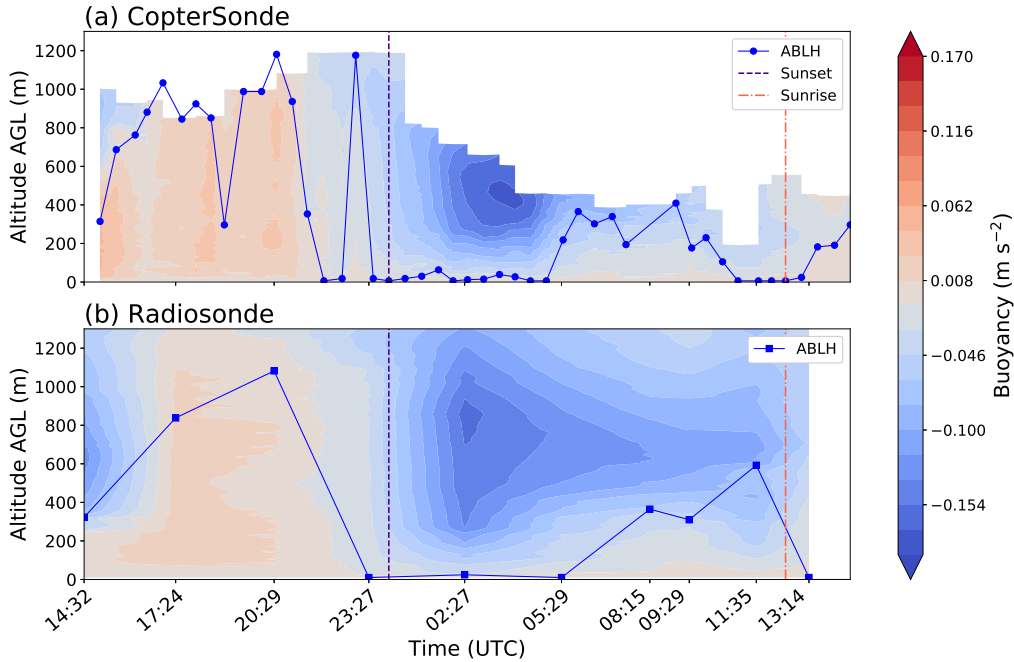
Figure 3.8: Same as Fig. 3.7 but with buoyancy field and buoyancy determined ABLD (blue line).

It is worth pointing out the differences in sampled potential temperature. Comparing the first radiosonde release and CopterSonde flight, the heights of mixed potential temperature disagree strongly (Fig. 3.2a, b). The depth of the mixed layer determined by a radiosonde release is around 330 m (Fig. 3.7b), while it is around 550 m for the CopterSonde (Fig. 3.7a). It is likely due to the radiosonde being advected downwind. Figure 3.2f shows 15-18 m s^{-1} winds in the 350-970 m layer. Between the 1430 UTC radiosonde release and the first CopterSonde flight at 1501 UTC, the radiosonde would likely be many kilometers downstream of KAEFS. The difference in mixing layer depths can also be seen in the buoyancy data (Fig. 3.2, 3.8). The shallow positive buoyancy

region found by the radiosonde leads to a much more negative vertically integrated buoyancy value compared to the nearest CopterSonde observation (Fig. 3.3).

The proposed buoyancy method is applied to both datasets, seen in Fig. 3.8. Unlike the CopterSonde derived heights using the potential temperature method (Fig. 3.8a), the buoyancy method provides more consistent, realistic heights. The 1724-2300 UTC time period has more agreement from profile to profile (Fig. 3.8a) as well as with the radiosonde derived heights (Fig. 3.8b). Furthermore, the radiosonde derived heights using the potential temperature method (Fig. 3.7b) and buoyancy method (Fig. 3.8b) are identical throughout the entire period. The correlation (r= 1.0) between the buoyancy method and the potential temperature method bolsters confidence that the buoyancy method is promising to determine ABLD. Once the jet arrives and mechanically mixes the surface layer, there is a rise in ABLD across all methods and datasets (Fig. 3.7, 3.8). Afterwards, the agreement between the potential temperature (Fig. 3.7a) and buoyancy (Fig. 3.8a) methods from CopterSonde data improves. As with most gradient methods, it suggests that the buoyancy method would perform better in convective boundary layers than stable boundary layers.
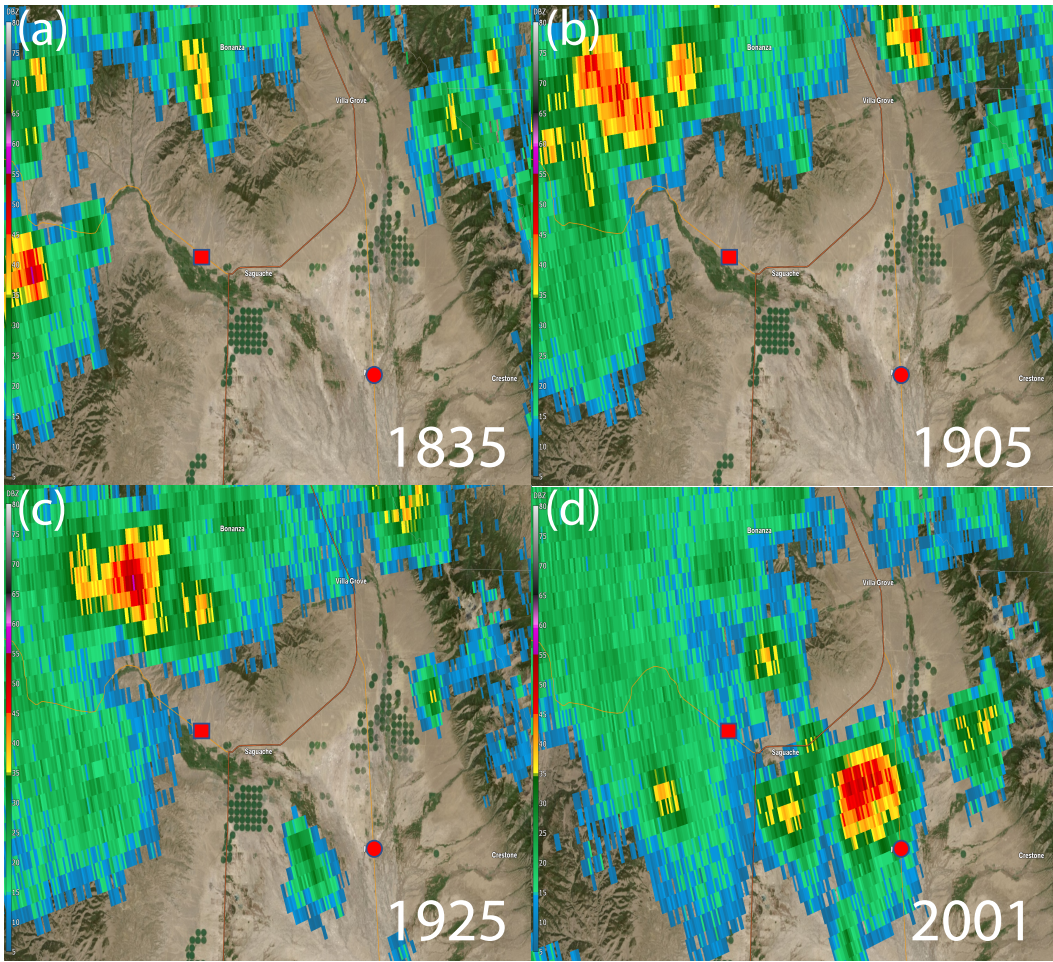
Figure 3.9: 0.5° level reflectivity (dBZ) from the KPUX radar in Pueblo, CO over the San Luis Valley on 15 July 2018. Red square indicates the K04V site and red circle indicates MOFF. a) 1835 UTC (1235 MDT) b) 1905 UTC (1305 MDT) c) 1925 UTC (1325 MDT) d) 2001 UTC (1401MDT)

3.1.3 Convective Initiation

Now, low-level buoyancy will be evaluated in a more traditional sense, under convective conditions. Buoyancy profiles within the San Luis Valley will be examined leading up to CI. This study will focus on 15 July 2018 since it experienced CI within the valley,

including directly over K04V (Fig. 3.10a). Fortunately, convection initiated over a profiling site, thus providing local discrepancies in pre-convective variables.

At 1715 UTC, the automated surface observing system (ASOS) stationed at K04V reported distant lightning and archived radar shows convection 25 km north of the site. Two hours later, the same ASOS station reported a thunderstorm. As a result, flights at K04V ended 30 min before flights at MOFF. At this time, the deepest convection was still 10 km north (Fig. 3.9c). A fundamental issue with radar coverage within the valley is that storms are not seen by the radar unless they are taller than the mountains. Around 1925 UTC, CI occurred 4 km east of MOFF. At 2001 UTC, the site only received light rain with stronger convection moving north. These times will become useful as we analyze the buoyancy and thermodynamic fields.
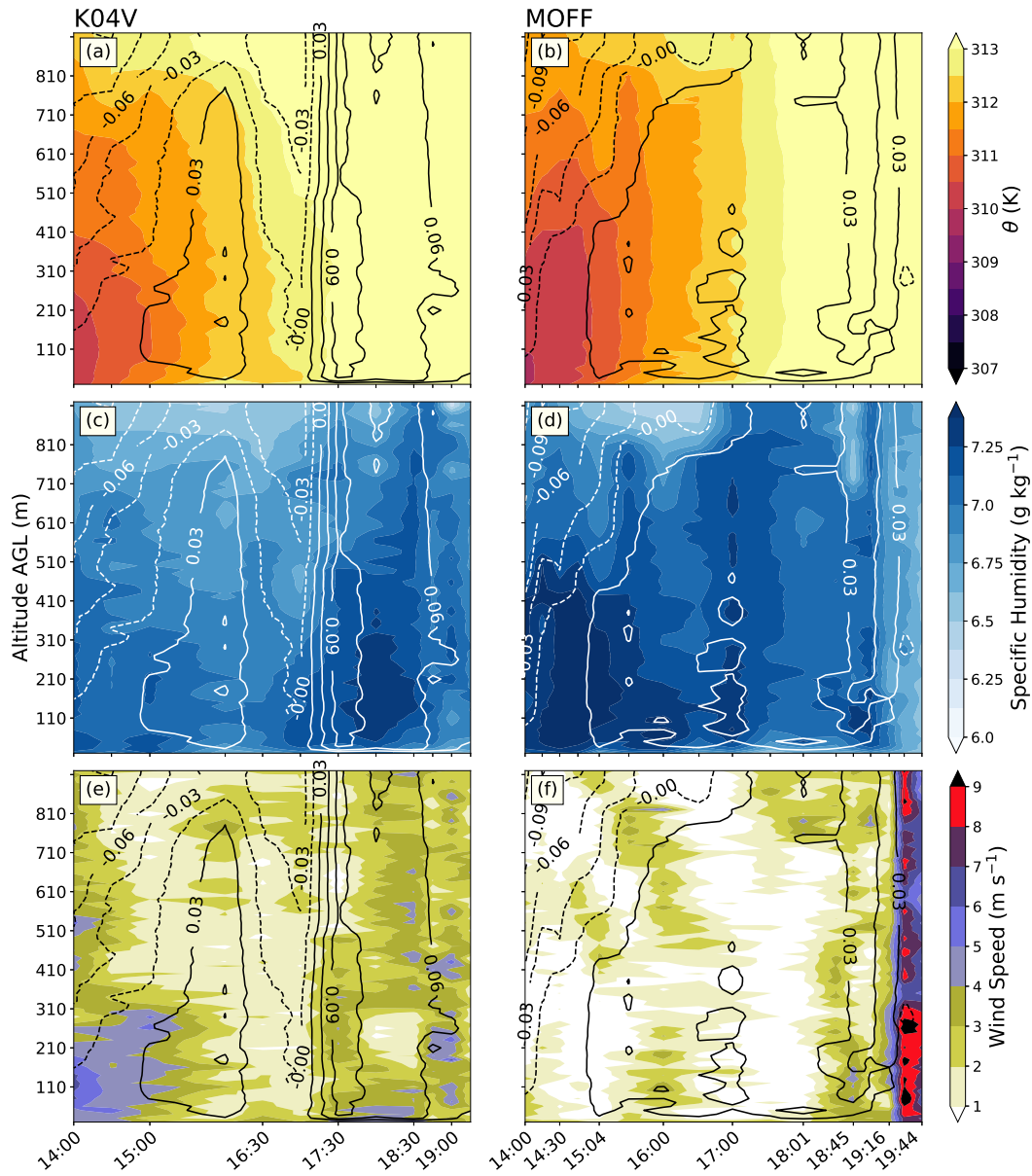
Figure 3.10: Same as Fig. 3.2 but on 15 July 2018 at the K04V site (a,c,e) and the MOFF site (b,d,f).

Figure 3.10a and 3.10b show how buoyancy and potential temperature evolve in time with height at both sites. The location of MOFF at the base of the valley leads to more moisture accumulation than within a sloped canyon. The drier air near the surface heats more quickly and leads to faster destabilization at K04V. From 1700-1740 UTC

there is a strong positive buoyancy gradient in time at K04V. Here, buoyancy is uniform throughout the entire layer. The amplified buoyancy is caused by a superadiabatic lapse rate beneath 30 m as seen in Fig. 3.11c. Since the warm layer is so shallow it is not visible in the potential temperature field (Fig. 3.10a). The 10-30 m range is especially steep surpassing the autoconvective lapse rate. The K04V ASOS data confirms a 4°C temperature increase from 1654-1736 UTC, not shown. As a result, overturning happens rapidly and the temperature is mixed slightly to reduce it by 1°C and weaken the lapse rate (Fig. 3.11d). This is short-lived and the autoconvective lapse rate returns 30-min later in Fig. 3.11e. During the overturning, the wind speed increases but is decreasing with height below 300 m (Fig. 3.10e). Autoconvective lapse rates induce turbulence within the layer to an unknown spatial degree. It seems to mitigate and regenerate the sharp temperature gradient on the order of 30 min. The random mixing dissipates energy gradually, delaying CI. It is clear that a superadiabatic lapse rate is not the only necessary component for CI since it did not occur for another 2 h after the first observation. Nevertheless, it aids in the distribution of moisture vertically.
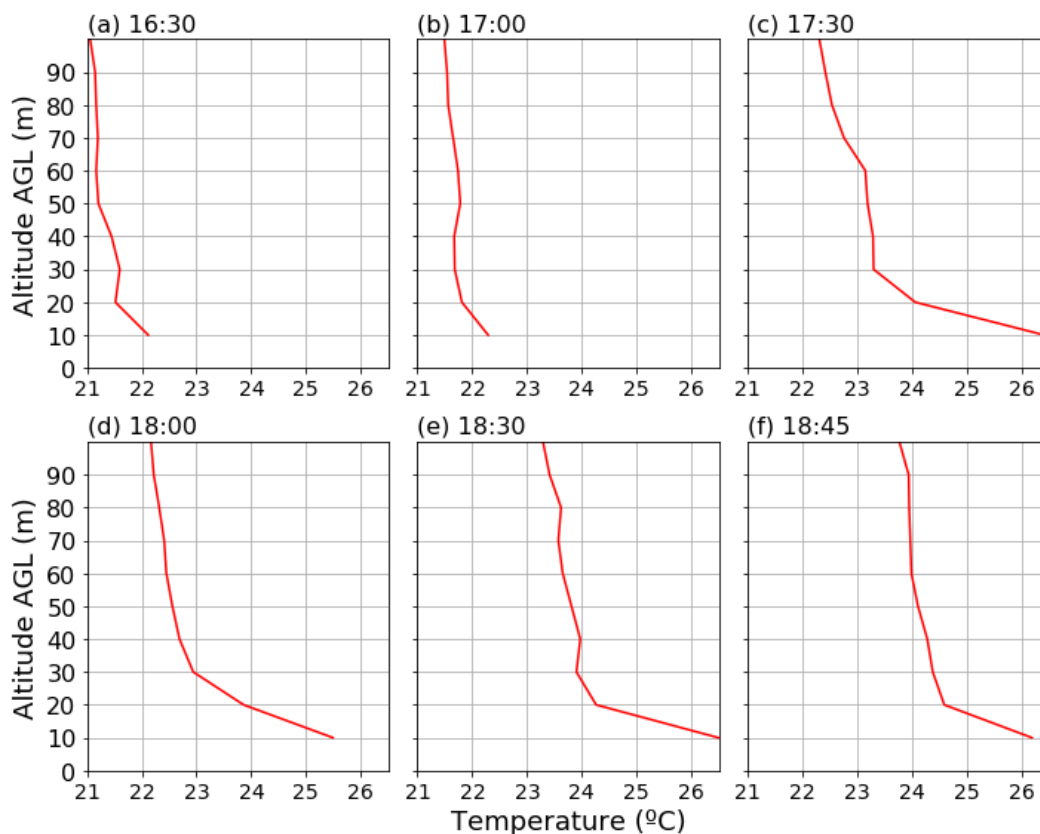
Figure 3.11: Temperature (°C) in the lowest 100 m from 1630-1845 UTC on 15 July 2018 at K04V.

Moisture is a necessary ingredient to CI. In the San Luis Valley, the distribution of moisture is often dynamic and influenced by many local factors. Synoptically, the moisture from monsoonal flow has come from mid-levels and mixed down towards the surface. In the morning, there is more moisture throughout the column at MOFF than K04V. As previously mentioned, the katabatic flow leads to a pool of moisture in the base of the valley. The declined slope of the Saguache Canyon reduces the overnight accumulation. However, the low-level moisture increases with time at K04V. A likely source of moisture is from the outflow from the storms to the north. The autoconvective overturning mixes the moisture throughout 0-500 m (Fig. 3.10c). Water

vapor continues to mix upward and persist throughout the remaining flights. Rapid destabilization coupled with deepening low-level moisture creates a favorable convective environment. Consequently, the K04V ASOS reports 14 m s^{-1} gusts from 1954 - 2030 UTC. Conversely, at MOFF there is little change in buoyancy and moisture decreases with time (Fig. 3.10a). At 1700 UTC there is a plume of moisture throughout 800 m coinciding with slightly higher buoyancy. Subsequently, there is drying throughout the layer. Once convection begins in the valley (2000 UTC), MOFF is drier and neutrally buoyant. As a result, the storm favors northward propagation, away from MOFF. The high wind speeds at 1944 UTC are from a strong outflow boundary due west of MOFF (Fig. 3.10f). While there was considerable lift, the buoyancy and moisture were not ideal to support CI.

Even though the two sites are only about 27 km apart, there is a difference in how buoyancy evolves in time, demonstrating its spatial sensitivity. Variations in moisture over the two locations change the rate of surface heating. Differences in moisture could be attributed to different land cover or different positions within the valley. Surface observations influence parcel trajectory, and buoyancy infers deviations about the environmental profile. Increased representation of land-air interactions is a valuable asset to any forecasting tool. Changes in moisture are further highlighted by buoyancy perturbations. A shift in surface temperature by a few degrees may be overlooked, but buoyancy accents how that affects the column. Overall, buoyancy in convective settings is sensitive to environmental changes, which may predate the amplification or weakening of convection.
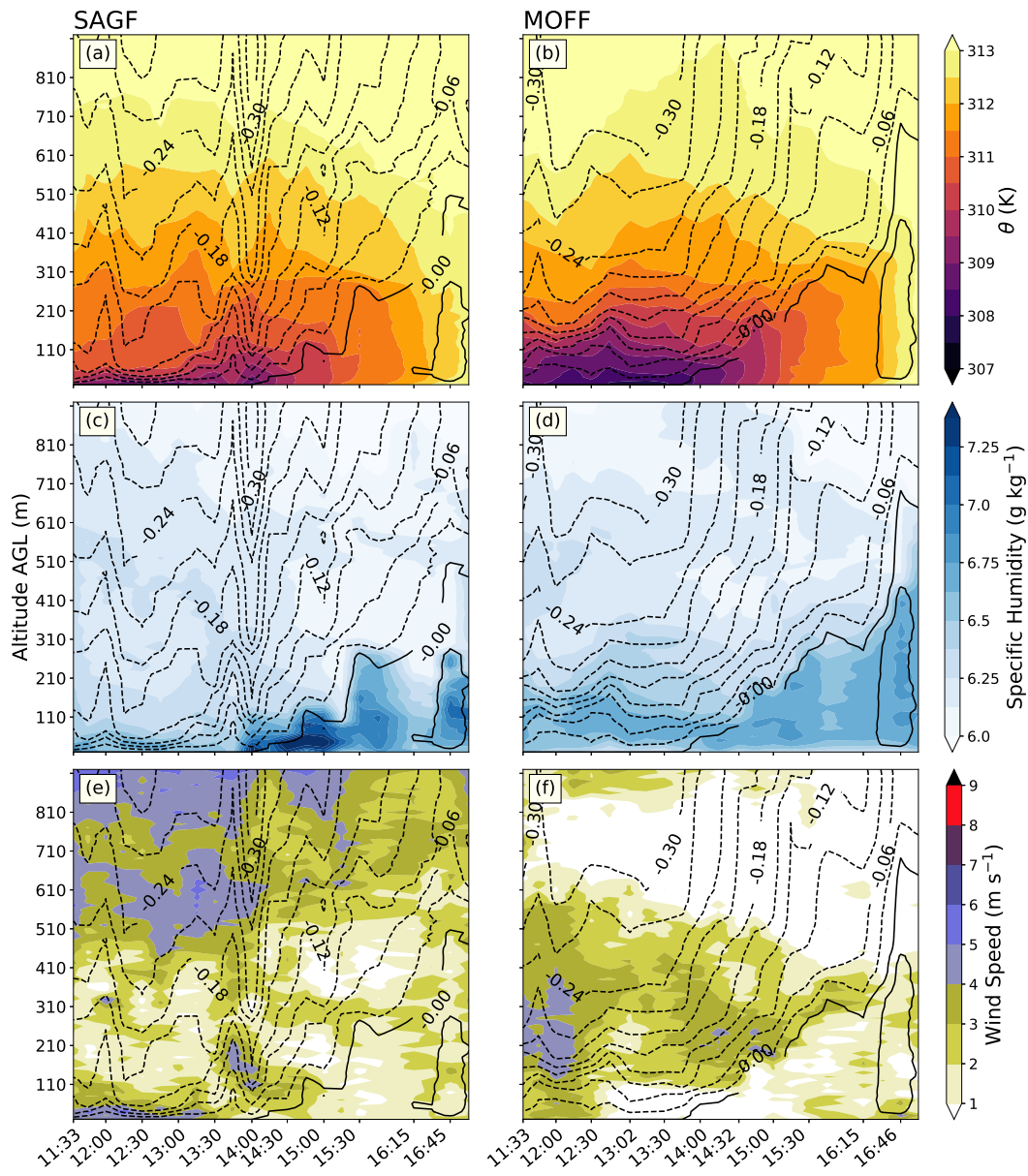
Figure 3.12: Same as Fig. 3.10 but for 19 July 2018.

3.1.4 Katabatic Flow

The final day of the campaign focused on cold air drainage since drying at mid-levels eliminated convective potential and radiative cooling was strong. The SAGF site is

deeper within the valley, thus allowing a cold pool to become more established compared to a sloped canyon. The time span of flights is also earlier to capture the full morning transition, starting 15 min before apparent sunrise (1148 UTC). SAGF is 18.25 km east southeast of MOFF, but the morning transitions are dynamically different.

Figure 3.12 focuses on the morning transition of state variables and buoyancy at both locations. Buoyancy aloft is predominantly negative and has a strong gradient in time and height. Radiative cooling causes the air above the surface to become denser and descend the valley walls. At MOFF, stratified layers are more apparent (Fig. 3.12b). On either side of the valley, there is downslope flow (Fig. 3.13). At SAGF, the flow is irregular below 500 m with light, variable winds which is likely due to closer proximity to the valley wall. In comparison, flow at MOFF is faster and uniform throughout 600 m for the first hour of flights. There is some directional wind shear from 1133-1215 UTC, leading to warmer air mixing down (Fig. 3.13b). After 15 min, there is a shallow stagnant layer below 100 m lending to increased cooling. The surface air temperature drops under the calm conditions (Fig. 3.12b). As a result, there is a stronger cold pool of air at MOFF than SAGF (Fig. 3.12a, b). At both locations, a strong temperature inversion settles in with subsequent negative buoyancy, although the magnitude of stability is different. Until 1400 UTC, MOFF has stratified layers up to 300 m. Meanwhile, the layer of stratification is only about 50 m deep at SAGF (Fig. 3.12c). Above that, the buoyancy fluctuates largely with time although the vertical gradient remains consistent. Within the shallow stratification, the winds are slightly faster (Fig. 3.12e). It is evident in the Ri profiles from each site that MOFF is more statically stable (Fig. 3.14). Predominantly, Ri is greater at MOFF due to weaker wind shear (Fig. 3.14). Stratification seems to be interrupted by the turbulent mixing caused by wind shear. In contrast, MOFF displays a textbook transition from morning

SBL to CBL. After the flow at MOFF is analyzed, the implications of turbulence on the flow at SAGF will be interpreted.
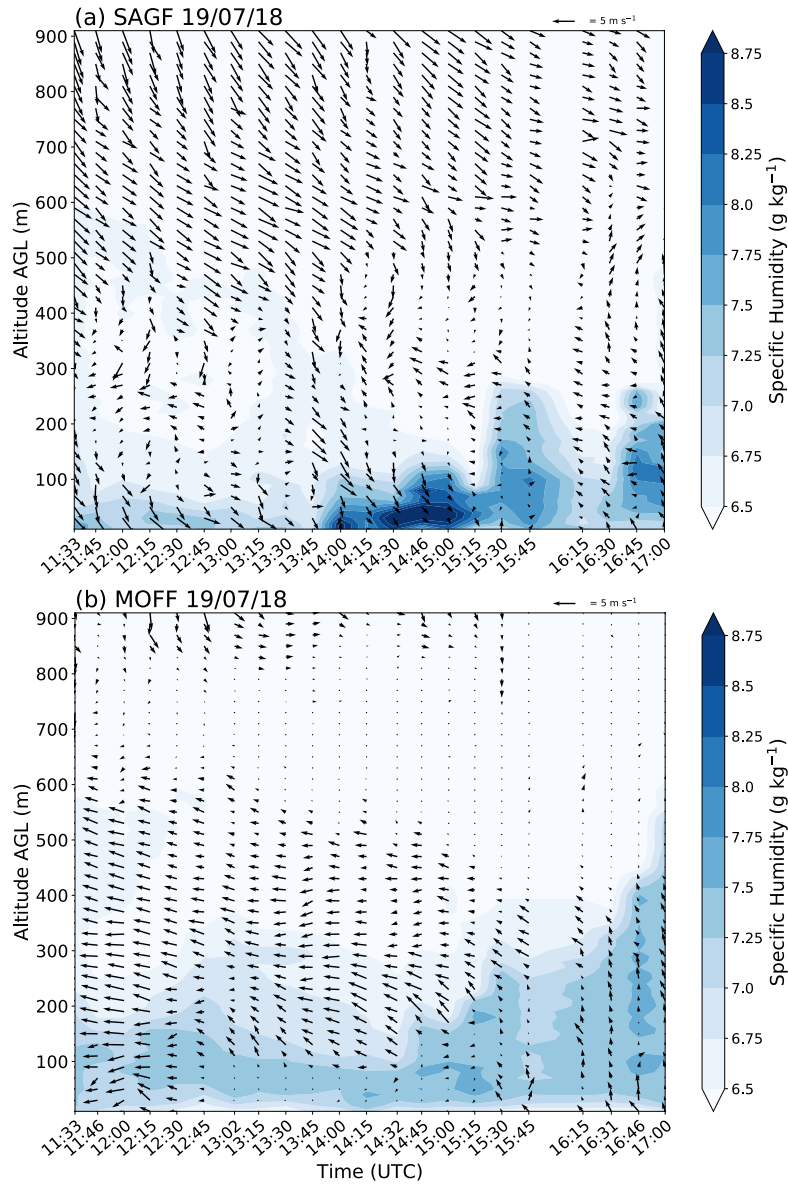
Figure 3.13: Wind vectors over specific humidity (g kg^{-1}) filled contours from Copter-Sondes on 19 July 2018 at (a) SAGF and (b) MOFF
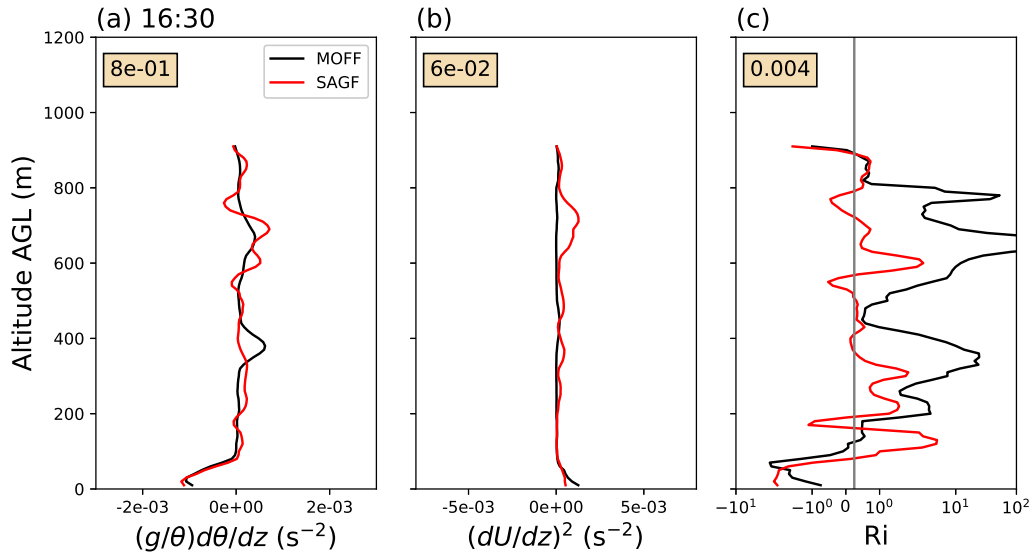
Figure 3.14: Similar to Fig. 3.5 but for 19 July 2018. Both are CopterSonde profiles at two sites, MOFF (black) and SAGF (red).

MOFF has a stronger cold pool and temperature inversion. There is very little wind shear until the CBL develops. In turn, the cold pool is colder and more homogeneous. The region of stratification aligns with a layer of moisture, such that the specific humidity decreases and becomes homogeneous beyond the same height that the buoyancy gradient decreases. At approximately 410 m the vertical gradient of buoyancy and specific humidity hit a local minimum and maximum, respectively (Fig. 3.12d). All of which suggests a transition to the residual layer. About an hour after sunrise (1245 UTC), the surface has warmed enough to dilute the density current, which causes the flow to slow within the lowest 100 m (Fig. 3.13b). Thereafter the surface warms, and a shallow mixed layer grows, but it is still capped by a stable layer. The region is convectively neutral with increasing mixed layer depth (Fig. 3.12). In the absence of moisture advection, the specific humidity illustrates vertical mixing. Not until 1530 UTC is the surface warm enough to initiate the southerly up-valley flow (Fig. 3.12, 3.13b). This

boundary layer transition is unlike either of the other cases examined. Since cold air pools into a thick layer at the base of the valley, the magnitude of stability surpasses what would occur from radiative cooling over flat land. The atmosphere reacts slower to incoming solar radiation to induce thermal mixing.

As for the SAGF site, the surface fluxes and position made the evolution more complex. Figure 3.12 contains more oscillations in buoyancy with time. These microscale buoyancy changes align with shifts in wind speed and moisture. The period of 1330-1415 UTC is of special interest; there is a defined buoyancy oscillation that aligns with a plume of moisture that is mixed upwards (Fig. 3.12c). Prior, there is a burst of stronger wind speed descending from 210 m to the surface from 1345-1445 UTC (Fig. 3.13a). Afterwards, the specific humidity rises by over 2 g kg^{-1}, and buoyancy has a positive rebound. Buoyancy is amplified and the CBL develops quickly. Low-level moisture is advected upwards in a nearly stepwise manner unalike to the gradual building of the CBL at MOFF (Fig. 3.12c, d). The 0.03 m s^{-1} buoyancy contours encapsulate the high moisture anomalies. With the moisture diffusion from the surface, the potential temperature begins to increase in a similar fashion to MOFF at 1545 UTC (Fig. 3.12a, b). Altogether, a turbulent event initiates a response across moisture and temperature which buoyancy precipitates, thus stimulating convective mixing and accelerating the SBL to CBL transition.
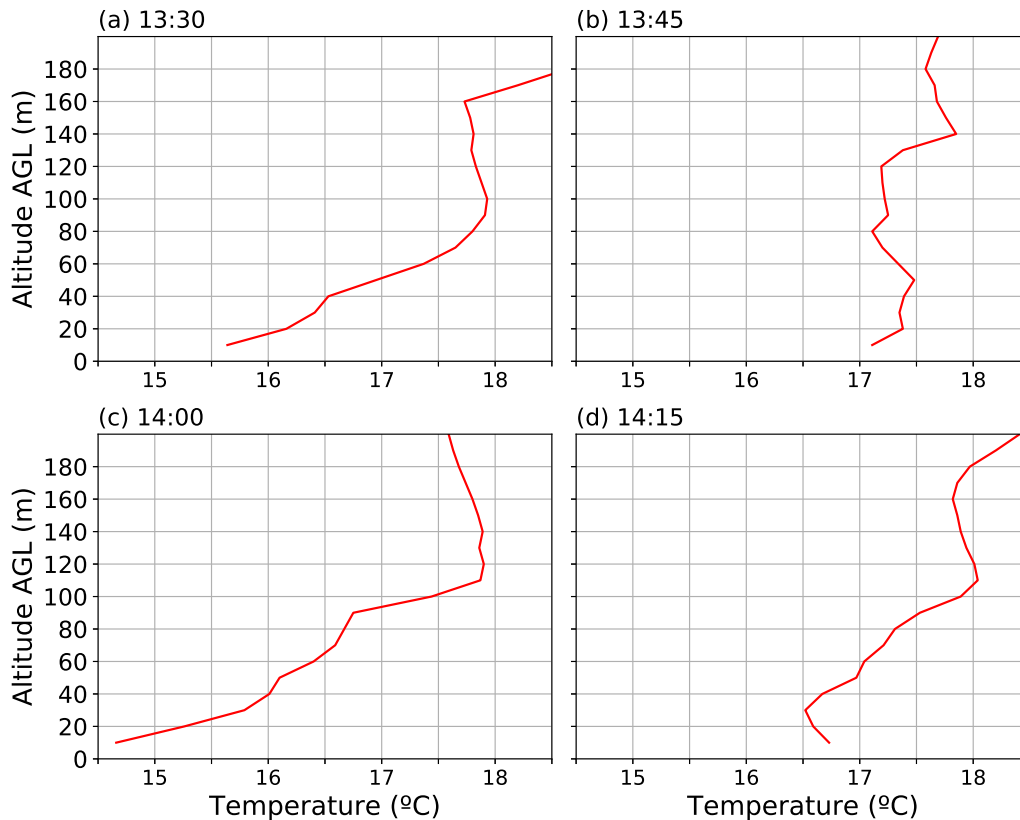
Figure 3.15: Same as Fig. 3.11 but for 1330-1415 UTC 19 July 2018 at SAGF.

It is plausible that a mountain wave initiated the kinematic response. The SAGF site is roughly 550 m downstream of the peak to the east northeast, based on the flow at that level (Fig. 3.13a). The advected turbulence reaches the irrigated fields 2 h after sunrise and triggers mass evapotranspiration. An injection of water vapor suddenly cools the surface air. Figure 3.15 shows that the surface temperature drops 2°C over 15 minutes, but the subsequent profile has the temperature rebounding back up 2°C. The temperature continues to climb even with another surge of moisture. With neutral conditions, the evaporative cooling is not confined to the surface, it is dispersed and temperature can rise as usual. Approximately 15 km south southeast of SAGF, Brus et al. (2021) finds evidence of transpiration as the number concentration of carbon

dioxide decrease and increase for water vapor from 1411-1642 UTC. As a whole, it takes a holistic view of meteorological conditions to dissect the causes and implications of the turbulent event. Nevertheless, low-level buoyancy highlights better than any single variable that there is a microscale land-air interaction.
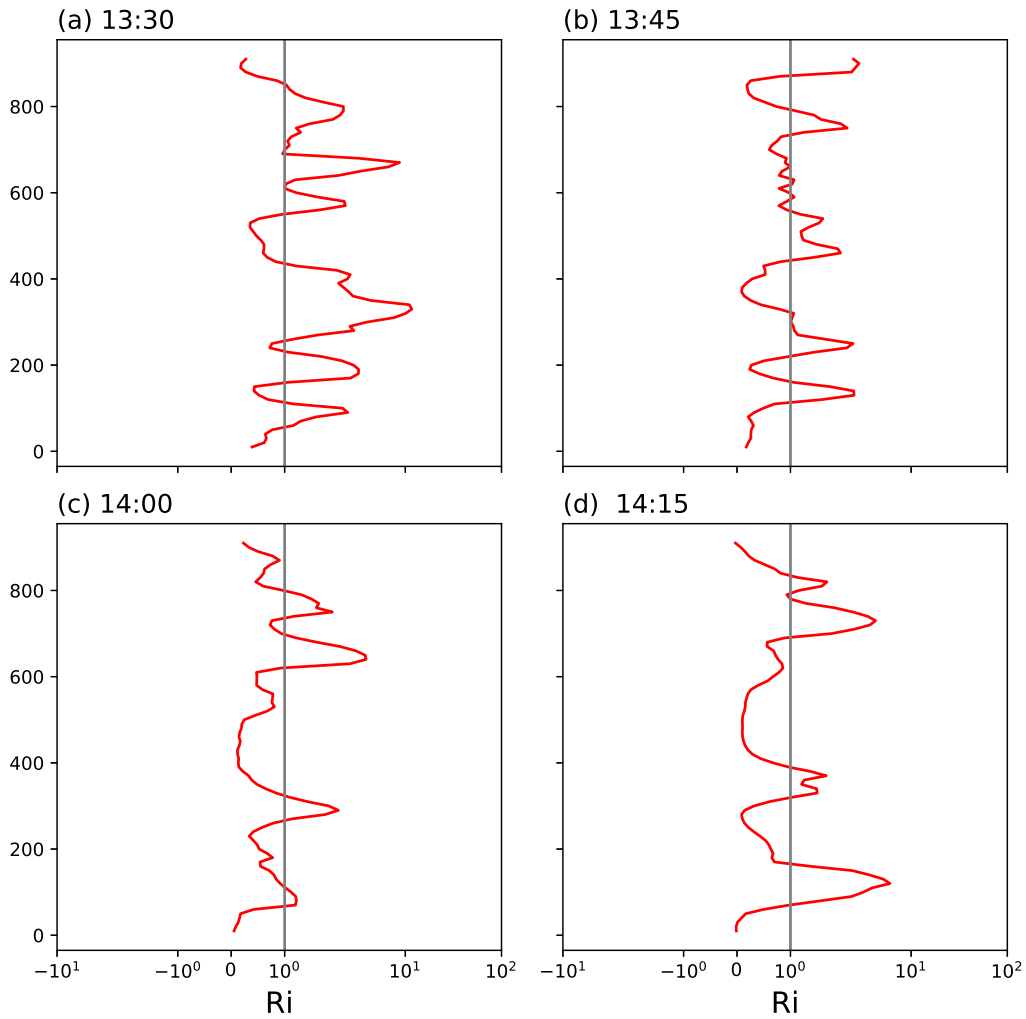
Figure 3.16: Ri profiles at SAGF from 1330-1415 UTC on 19 July 2018. Gray line indicates $Ri{=}1.0$

Since Monti et al. (2002) determined there is an stronger correlation to increased TKE when $Ri < 1.0$ than $Ri < 0.25$, the following analysis will use $Ri_c = 1.0$. Figures

3.16c and d 3.16 indicate an increase in subcritical Ri layers after 1400 UTC. Near the surface, Ri is below Ri_c across all times but in a deeper layer after 1330 UTC (Fig. 3.16). The clearest evolution to more turbulent flow is in the 300-600 m layer. At 1415 UTC, a layer of stable flow forms as the winds become more homogeneous from 100-190 m while the subcritical layer extends vertically to 400-700 m (Fig. 3.12e, 3.16d). The turbulent layer appears to move vertically with time as the layers beneath mix. While Ri profiles accentuate how different layers are affected by overturning, in the absence of the previous analysis using buoyancy, it would be difficult to identify what exactly occurred. Overall, the evolution of Ri is not indicative of injection or turbulent dispersion of an evapotranspiration plume. Since Ri does not factor in moisture, it lacks those impacts altogether. In the context of this environment, Ri profiles do not offer enough information as is needed to fully describe the dynamics.

Evapotranspiration is a valuable piece of knowledge for farmers. It factors into decision-making for watering and harvesting. There is only a 15-min period between the buoyancy perturbation and its impacts, so the prospect of using it as a forecasting tool in real-time is not feasible. From a modeling perspective, buoyancy could lend aid to enhancing land-air feedback parameterizations. More broadly, the high-frequency moisture data could be very beneficial for quantifying water transfer from evapotranspiration. Using buoyancy under these circumstances is rather novel. Throughout turbulence equations, buoyancy is viewed as a sink under stable conditions. In the case shown, negative buoyancy anomalies can present a turbulent source. Meaningful interpretations of buoyancy, negative or positive, offer new opportunities to connect land-atmospheric interactions throughout the ABL.

Chapter 4

Operational RPAS Application

4.1 Aviation Weather Background

Pilots of RPAS and crewed aircraft alike can be impacted by the ABL data gap during takeoff and landing. Airports are often outfitted with ASOS, but these observations tell little about conditions above the surface. Terminal radars are useful in detecting precipitation, but may not always accurately determine precipitation type. Additionally, scatterers, which are not always present, are required to collect Doppler velocities. All of these factors can leave pilots without knowledge of low-level wind shear or icing potential beyond the surface. Furthermore, the spatial homogeneity of these measurements may be constrained in the presence of complex terrain. On a different note, RPAS's battery life and connectivity are sensitive to temperature and humidty which can change over short timescales in the ABL. The type and size of RPAS influence the weather impact on the system (Ranquist et al., 2017). Presently, the FAA requires crewed flights to have a weather assessment prior to takeoff, while the preflight check for RPAS is less rigorous. RPAS preflight requirements are based on maintaining a visual line of sight but do not encompass weather hazards. Nevertheless, ensuring a safe mission requires a complete weather assessment. It would be nearly impossible to employ an observational network everywhere an RPAS would fly, so the obvious progression is tailoring NWP to RPAS scale processes.

As commercial RPAS use increases, the need for RPAS specific forecasts is necessary. There has been a handful of studies completed to research operational needs for RPAS. Campbell et al. (2017) describes a plan addressing weather information gaps, impacts, and avenues to research. Lundby et al. (2019) offers an RPAS weather forecast framework to estimate how often weather conditions would implicate flights based on surface observations. Risk models will require high-resolution weather model input (Roseman and Argrow, 2020), but operational NWPs lack the resolution to accurately simulate microscale features. Roseman and Pinto (2019) discuss the current resources available to RPAS pilots while conveying their shortcomings. They also discuss the goals in designing a high resolution (100 m) large eddy simulation (LES) to aid RPAS forecasts. Pinto et al. (2021) tested the concept by running LES to aid forecasts for the LAPSE-RATE field campaign (de Boer et al., 2020b). The model successfully captured flow features and ABL transitions with 111 m grid spacing. Jensen et al. (2021) show that forecasts are benefitted by assimilating RPAS data into a slightly coarser (1 km) model. Thus, it was confirmed to be feasible to adjust numerical models to the needs of RPAS.

To avoid flying in restricted airspace and over people, RPAS flights are often in remote areas which may offer little weather data. One avenue is to have a specific weather sensing RPAS, as mentioned in the introduction, work in tandem with other specialized RPAS. It would gather data prior to deployment and be used for flight planning considerations. It could also be assimilated into a numerical model to improve ABL representation. Another possibility is outfitting the RPAS with weather sensors so data could be collected throughout the flight, similar to larger commercial aircraft. Although, this could add too much weight for small RPAS. Either method would address the NASA UAS Traffic Management (UTM) goals to increase situational awareness for crewed and uncrewed aircraft. This chapter will highlight how regular

profiles from a weather sensing RPAS could benefit conventional, crewed pilots at a small airport. Furthermore, it highlights the cooperation and communication needed to make flying an RPAS at an active airport possible.

Figure 4.1: Launch site at KOUN with active runway behind the building. Photo credits to Bill Doyle.

4.2 Concept of Operations

The Max Westheimer Airport (KOUN) is a Regional Business Airport in Norman, Oklahoma owned and operated by the University of Oklahoma. KOUN is an integral component of the School of Aviation. It is in Class D airspace and operates under the guidance of an air traffic control (ATC) tower. There is a miniature runway with the same layout as the primary which lies southeast of the terminal. This location has few nearby obstructions and is within line of sight from the ATC tower, making it the ideal location for CopterSonde profiles, as seen in Fig. 4.1. It is worth noting that the visual from the ATC tower is no substitute for a nearby visual observer who is meant to keep eyes on the RPAS at all times. The goal is less for ATC workers to see the CopterSonde during a flight but to see the crew operating. There is also a radio set up between the RPAS crew and the ATC workers. The COA flight ceiling is at 3,000 ft AGL, but above 1,800 ft airspace changes to Class E and the Oklahoma City terminal radar approach control facilities requires notification prior to operations.
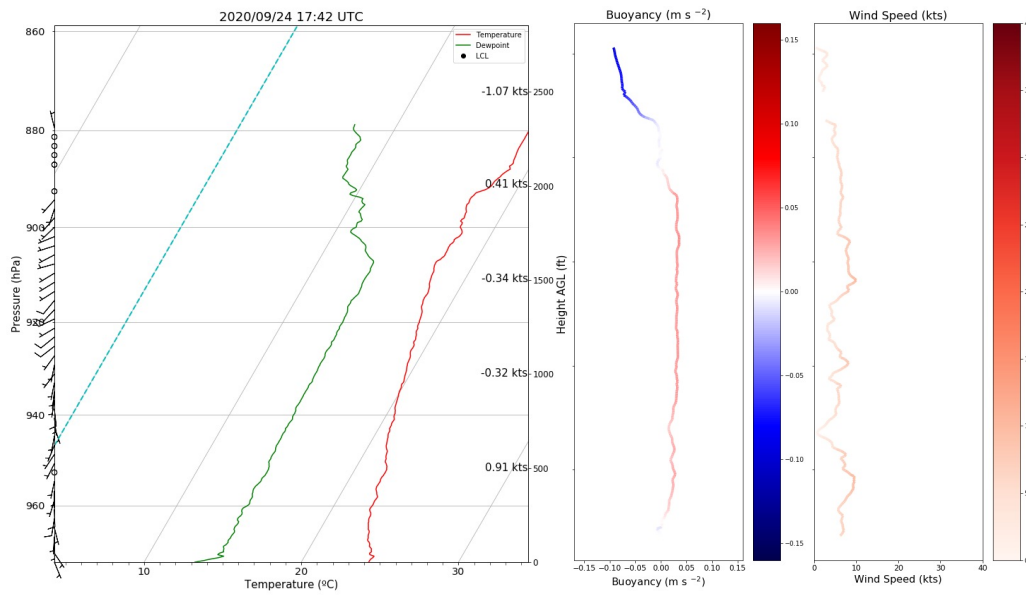
Figure 4.2: (left) Skew-T log-p diagram of conditions sampled by the CopterSonde at KOUN at 1724 UTC 24 September 2020. Blue dashed line indicates the 0°C isotherm. (center) Verical profiles of buoyancy (m s^{-2}) and (right) wind speed (kts).

Numerous discussions between a multidisciplinary team of meteorologists, ATC operators, pilots, and aviation professors were held prior to flights at the airport. From these talks, we gathered what information would be beneficial to the pilots and discussed the ideal presentation and accessibility. On 24 September 2020, flight conditions were calm with scattered clouds as three vertical CopterSonde profiles were successfully collected. Discussions after initial operations presented other steps that should be incorporated to optimize safety and communication. The resurgent COVID-19 pandemic interrupted progress to integrate profile collection into operations. The intent was to train School of Aviation students to fly the CopterSonde and gather a daily profile at 1500 UTC. The CASS team would promptly process the data and upload a visualization accessible by a monitor in the existing weather information area. The data processing is to follow the same techniques described from the Flux-Capacitor

campaign with 3 m vertical spacing. The concept of operations is in place to integrate RPAS flights at KOUN. This setup does not have to be unique. Given the proper authorizations, communications, and platforms, RPAS can work symbiotically in aviation weather to improve awareness of near-surface hazards.
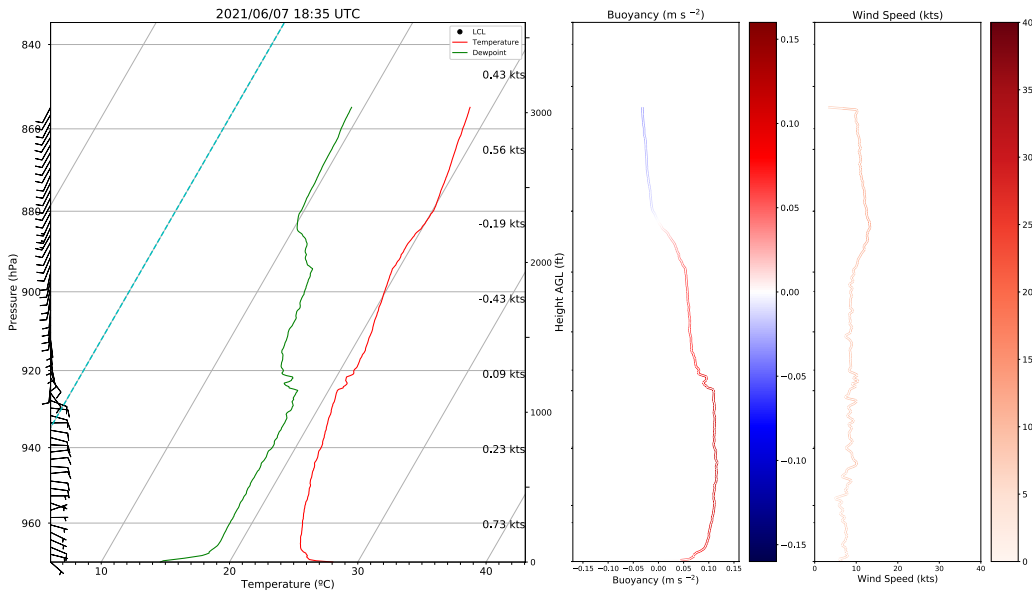
Figure 4.3: Same as Fig. 4.2 but at KAEFS at 1835 UTC 07 June 2021.

4.3   Data Examples

Figure 4.2 combines the desires of both pilots and aviation forecasters. The skew-T log-p format is generally well understood amongst pilots in the program. Due to the lack of flights at KOUN, profiles from KAEFS are used to supplement the analysis. The following section will use past profile data to discuss key aviation hazards in the context of preflight preparations.

Freezing conditions aloft could pose icing concerns especially if the surface temperature is above freezing. Surface observations, such as ASOS, would not provide the necessary information for icing forecasts. The dashed blue line indicates the freezing

line. If the temperature at any level dips below 0°C, a message will appear informing pilots that ice may be possible. Timely temperature profiles are necessary to predict the precipitation type. Tripp et al. (2021) demonstrates the utility of the CopterSonde in forecasting winter weather. Even though the CopterSonde has a limited flight ceiling, it transects a freezing layer which would be conducive for a significant icing threat (see Fig. 6 in Tripp et al. (2021)). Mixed-phase precipitation is particularly difficult to forecast since precipitation type can change on the order of tens of minutes (Reeves, 2016). The operational release times of radiosondes are insufficient to monitor changes on that scale. It should be noted that the CopterSonde is also prone to icing and does not have a deicing system. The impacts of icing on measurements have not been quantified, ergo the CopterSonde operator should take the same precautions of any conventional aircraft and avoid operating in icing conditions as much as possible.
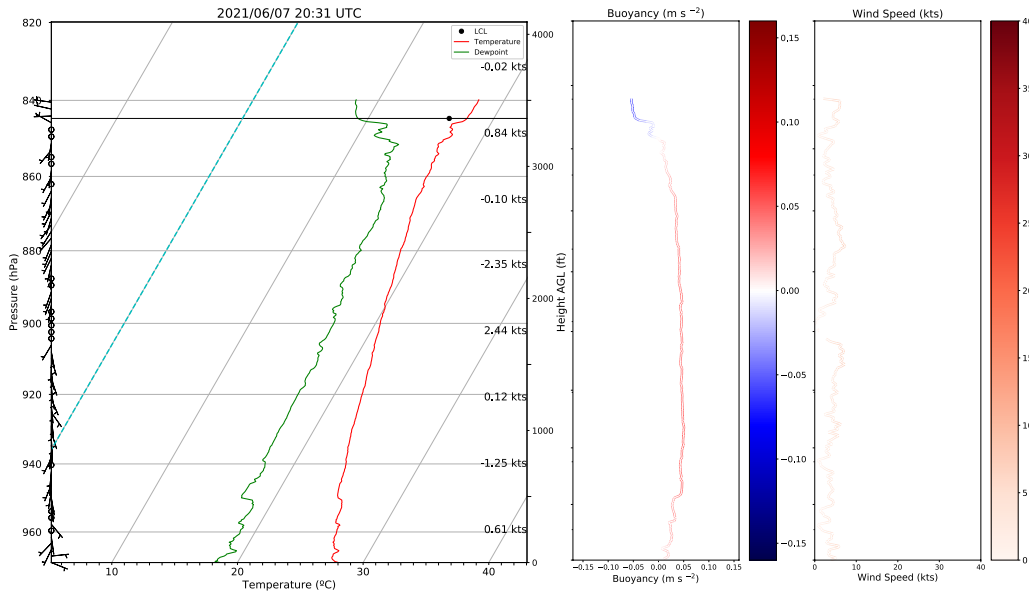
Figure 4.4: Same as Fig. 4.3 but at 2030 UTC

The lifting condensation level (LCL) is demarcated with a black line and dot. The LCL is a good estimator for the cloud base. Knowledge of the cloud base is critical

for RPAS which must remain in visual line of sight and out of clouds. Under a CBL, cumulus clouds can form rapidly at the LCL and occlude visibility. Cloud formation is typically tied to thermal ascent which may induce turbulence. Similar to the ABL depth, often the LCL extends beyond the flight ceiling of the CopterSonde. In order to keep the graphics simple, the LCL is excluded if it surpasses the maximum altitude.
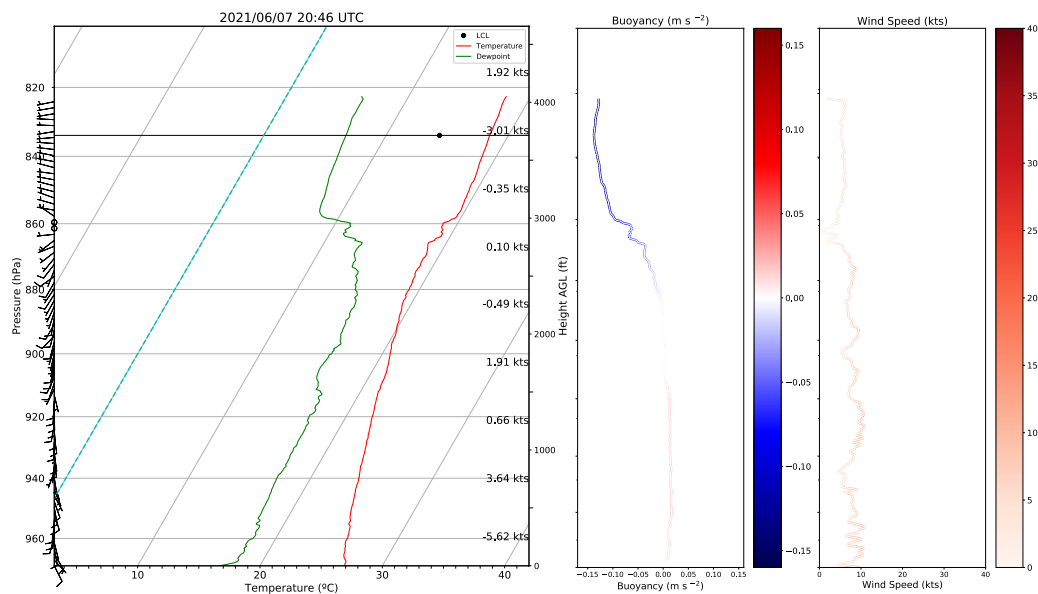
Figure 4.5: Same as Fig. 4.3 but at 2046 UTC

Low-level turbulence (LLT) is another common hazard for aviation. Since LLT is usually mechanically or thermally induced, supplemental plots of buoyancy and wind speed are provided (Fig. 4.2). Indicators of LLT allow pilots to plan for issues with takeoff or landing. While this is not the case for KOUN, airports in complex terrain can experience orographically driven mechanical turbulence. Instances of terrain-influenced LLT are seen in the LAPSE-RATE campaign. During the cold-air drainage transition, there is both directional and speed shear (Fig. 3.13a). Strong wind shear can generate turbulence over flat land with decreasing intensity away from the surface, leading to problems with climb speed or landing distance. Figure 4.5 shows a case with vertical

speed shear as well as directional variability. Another benefit of the wind speed profile is it highlights a jet even though the shear is low due to a steady logarithmic increase in speed (Fig. 4.6). The standard shear layer depth is 500 ft but can be tailored to meet the needs of the aircraft. The wind barbs on the lefthand side of the Skew-T visualize the directional shear. Although the winds are light, the directional shear indicates changes in air mass properties, as seen in Fig. 4.3. There is a decrease in moisture and a nearly isothermal layer above the level where the winds shift from easterly to southerly.
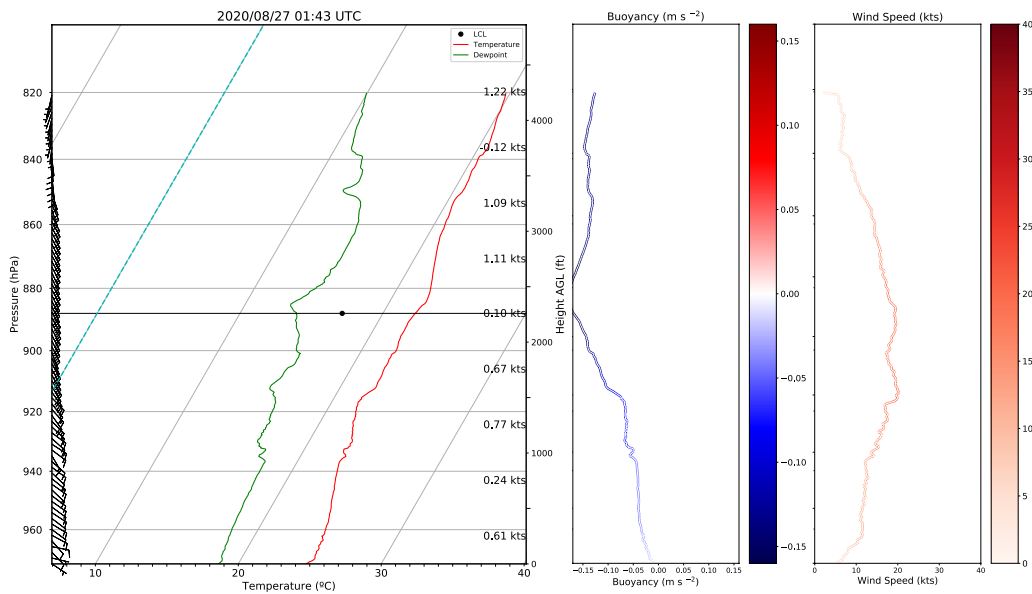
Figure 4.6: Same as Fig. 4.2 but at KAEFS at 0143 UTC 27 August 2020

Figure 4.4 shows a very buoyant, mixed layer. The winds are light and variable in the lowest 100 m (Fig. 4.4). The lapse rate is not as steep as it was earlier (Fig. 4.3). These factors combined with the slight variation in the temperature profile suggest some turbulence near the surface. Towards the top of the profile, a stepwise transition from a positive to negatively buoyant atmosphere differs from the smooth transitions seen elsewhere, indicating some mixing going on near the top of the ABL (Fig. 4.4).

The following flight displays evidence of entrainment. Figure 4.5 has a pronounced wind shift and decrease in moisture at 860 hPa. The neutral buoyancy layer is much deeper and at a lower elevation than 15 min prior (Fig. 4.4). As the stable air from the free atmosphere is mixed into the CBL, the buoyancy is reduced. Even without multiple profiles, fluctuations in the buoyancy profile can suggest that turbulent eddies may be induced. Since the entrainment zone is intermittently turbulent, altitude indicators of the entrainment zone could benefit pilots. Given that a common definition for the entrainment zone altitude is an inversion of buoyancy flux, the buoyancy profile can provide a rough estimate (Deardorff et al., 1980).

4.4   Discussion

There are numerous obstacles to overcome to institute regular RPAS profiling at an active airport. Adding an RPAS in a live airspace can add conflict and requires enhanced situational awareness. Some pilots may be wary of crowding airspace for additional observations. A streamlined process would help to gather observations as few times as necessary and as efficiently as possible. Flights should be timed when there is no active takeoff or landing. Even though a 1 km profile takes less than 15 min., it would be difficult to accomplish at a major airport. An early morning profile could be taken before the arrivals begin. Observations of morning conditions are instrumental to understand winter conditions. Depending on the environment, more flights may need to be incorporated at different points throughout the day. Ideally, flight plans would be laid out at least 24 h in advance and would be coordinated around crewed flight schedules.

Moreover, the greatest need for observations is in environments with the most risk. The process of deciding the cost-benefit of flying in potentially hazardous conditions

would need to be objective. Training sessions would benefit the communications between the RPAS team, pilots, and ATC operators. This leads to the question of who would standardize this process? There are many inherent dangers that come with adding an RPAS to a live airfield, so actions must be pre-meditated and taken with an abundance of caution to ensure the safety of crewed flights. Any incident could halt all authorizations to fly and impede any further progress.

For all of the reasons listed above, the FAA rarely authorizes RPAS COAs in controlled airspace. The addition of Remote ID and Automatic Dependent Surveillance-Broadcast (ADS-B) improve awareness for all pilots. ADS-B out technology notifies nearby aircraft and ATC of the RPAS's location and heading. The process to get the COA around KOUN approved still took months of discussions and compromises. A three-person crew composed of a pilot in command, visual observer, and ground station operator is the minimum size. The question of who will crew the system becomes an obstacle. For our team, this was a huge setback. Without the bandwidth to crew or to train others, as envisioned, the operations fell to the wayside. Our goal was to train student pilots to operate as the crew since they would already have the license and be at the facilities. KOUN is a unique, learning airport with a steady supply of pilots with flexible schedules. Outside of this space, whose shoulders does this task fall to? Not to mention, the RPAS needs regular maintenance and repairs. Without access to a facility, there could be major delays in operations. The practicality of operations requires an immense level of infrastructure which is beyond the scope of this paper. While the FAA has instituted many initiatives and task forces to increase UTM, it may fall to a private sector company to facilitate the integration of RPAS into airport operations.

Another necessary component to the success of this program is communicating the importance of the data to pilots. Pilots need the tools to analyze the meteorological

data in a way that is helpful but not overwhelming. In one of the conversations, a pilot stated that he rarely looked at atmospheric soundings. Even though many of their requests for wind shear and thermodynamic profiles could be found there. A dedicated social science analysis on how pilots ingest weather data would be beneficial to integrate the new data product into the preflight process. The UTM mission cannot succeed if the audience it should help the most does not understand it. The analysis performed in this paper can act as a guide to interpreting some key conditions but is far from all-encompassing.

Chapter 5

Conclusions and Future Work

This study uses buoyancy measured from RPAS to describe transitions within the ABL. Different cases with and without mesoscale forcings are evaluated to understand the versatility of using low-level buoyancy. Recent developments in weather sensing RPASs allow for high-frequency sampling within the ABL. The spatial and temporal sensitivity of buoyancy allows for a more detailed interpretation of fine-scale processes. Buoyancy becomes convectively mixed like potential temperature below the capping inversion, such that the maximum height of constant buoyancy appears to transition with the ABLD(Fig. 3.2, 3.10).

The application of vertical buoyancy gradients to derive the ABLD shows promising initial results. The potential temperature and buoyancy method derived heights perfectly correlate (r= 1.0) when radiosonde data are used. The correlation from the two methods, using CopterSonde data is not as strong (r= 0.45). Although, the buoyancy method heights are comparable to the heights derived from the radiosonde data. These heights agree better across methodologies with the radiosonde data than the potential temperature method with different data sources. Inherently, more cases need to be evaluated to have full confidence in the method. Moreover, there are avenues to improve the buoyancy method, particularly when using the CopterSonde data. The high vertical resolution leads to noise in the profiles that is erroneously picked up as the ABLD. Logical arguments will be applied to reduce inconsistencies in ABLD for consecutive flights. Also, a technique to exclude the surface layer transition to the

mixed layer should be developed. The success of this simple method gives credence that with proper improvements it could become a trusted ABLD definition.

The versatility of buoyancy is highlighted in different environments. Figure 3.2e and 3.2f display a negative buoyancy gradient beginning two hours before the jet arrives. Negative buoyancy is in accordance with traditional findings of a stable boundary layer during nocturnal LLJ (Blackadar, 1957b). In the San Luis Valley, Fig. 3.10b shows an acceleration in positive buoyancy leading up to CI. This agrees with Trier et al. (2014) that there is rapid destabilization before CI, quantified by parcel buoyancy. MOFF has weaker buoyancy (Fig. 3.10a) and results in shallower convection than K04V. During katabatic flow, buoyancy reacts to the sudden injection of water vapor from evapotranspiration (Fig. 3.12c, e). Buoyancy aligns with the induced turbulence of this event better than potential temperature (Fig. 3.12a, e). Further investigation is required to see if these results are reproducible at other times. Increased data collection from RPAS across multiple field campaigns will generate a database of profiles ranging in conditions. Then, statistical analysis can be performed to determine if there is a correlation between the rate of change of buoyancy and events such as CI or LLJs.

On the other hand, Ri profiles from the CopterSonde are less attuned to environmental changes. Firstly, processing Ri profiles is nontrivial and has room for improvement. The incomparable data processing of radiosondes and the CopterSonde profiles made it difficult to make objective decisions on smoothing techniques. Due in part, the CopterSondes wind components are much noisier than the radiosondes. The CopterSonde profiles during and following the LLJ have very little difference, which is partially faulted to the limited flight ceiling (Fig. 3.4). The Ri profiles give little information to show the turbulent downward mixing from the jet in the region below the jet. Similarly, this occurs with the katabatic flow case. Figure 3.16 indicates a much shallower layer of turbulent flow (Ri<0.25) than seen in Fig. 3.12. In short, the

CopterSonde's abilities are not exemplified using Ri profiles in the cases evaluated. It could be that the right data processing was not chosen, or that the wind data collection method is not suited for calculating a turbulent parameter such as Ri.

There is potential for buoyancy to evaluate many other microscale to mesoscale processes. Measurements taken along a dryline could increase understanding of where horizontal convective rolls occur. Horizontal convective rolls are conducive for CI due to vertical motion and thermodynamic gradients described in Weckwerth et al. (1999). Sea-breeze fronts advect moist, cool air which adds stability to the layer while also providing lift. Sea-breeze fronts often induce CI, but the exact location and why are still unknown. Since buoyancy is sensitive to the changes in temperature profiles, it could be fruitful to look at the buoyant evolution with the passing of a sea-breeze front. It becomes even more complex when the sea-breeze collides with a large urban sprawl. RPASs can fill a gap in measurements in urban settings to increase understanding of turbulence and aerosol transport. Buoyant plumes transport aerosols throughout the city, but measuring this typically requires non-permanent towers and tracers, such as smoke or colored aerosols. RPASs deployed to determine buoyancy within the urban canopy could help improve air quality predictions. The applications for low-level buoyancy go beyond the topics evaluated in this study. Meanwhile, RPASs can collect measurements during processes that are not easily accessible. Together they can help address processes not adequately realized.

Regular RPAS profiling opens avenues to understand microscale interactions within the ABL. RPAS can also aid in aviation forecasting if profiling sites can be established at airports. Buoyancy is just one variable that has shown use in describing the state of the ABL, which was not previously accessible. Buoyancy is sensitive, physical, and simple. This study is a simple starting point to revive a classically defined variable in light of new technology. Buoyancy measured by RPASs can describe ABL transitions

with little computational power while providing more information than traditional ABL variables.

Reference List

Anurose, T. J., and D. B. Subrahamanyam, 2015: Evaluation of ABL parametrization schemes in the COSMO, a regional non-hydrostatic atmospheric model over an inhomogeneous environment. *Modeling Earth Systems and Environment*, **1 (4)**, 38, doi:10.1007/s40808-015-0045-y, URL https://doi.org/10.1007/s40808-015-0045-y.

Astling, E. G., J. Paegle, E. Miller, and C. J. O'Brien, 1985: Boundary layer control of nocturnal convection associated with a synoptic scale system. *Monthly Weather Review*, **113 (4)**, 540–552, doi:10.1175/1520-0493(1985)113⟨0540:BLCONC⟩2.0.CO; 2, URL https://journals.ametsoc.org/view/journals/mwre/113/4/1520-0493_1985_113_0540_blconc_2_0_co_2.xml, publisher: American Meteorological Society Section: Monthly Weather Review.

Balsley, B. B., R. G. Frehlich, M. L. Jensen, and Y. Meillier, 2006: High-resolution in situ profiling through the stable boundary layer: Examination of the SBL top in terms of minimum shear, maximum stratification, and turbulence decrease. *Journal of the Atmospheric Sciences*, **63 (4)**, 1291–1307, doi:10.1175/JAS3671.1, URL https://journals.ametsoc.org/view/journals/atsc/63/4/jas3671.1.xml, publisher: American Meteorological Society Section: Journal of the Atmospheric Sciences.

Balsley, B. B., D. A. Lawrence, D. C. Fritts, L. Wang, K. Wan, and J. Werne, 2018: Fine structure, instabilities, and turbulence in the lower atmosphere: High-resolution in situ slant-path measurements with the DataHawk UAV and comparisons with numerical modeling. *Journal of Atmospheric and Oceanic Technology*, **35 (3)**, 619–642, doi:10.1175/JTECH-D-16-0037.1, URL https://journals.ametsoc.org/view/journals/atot/35/3/jtech-d-16-0037.1.xml, publisher: American Meteorological Society Section: Journal of Atmospheric and Oceanic Technology.

Banta, R. M., Y. L. Pichugina, and R. K. Newsom, 2003: Relationship between low-level jet properties and turbulence kinetic energy in the nocturnal stable boundary layer. *Journal of the Atmospheric Sciences*, **60 (20)**, 2549–2555.

Bell, T. M., B. R. Greene, P. M. Klein, M. Carney, and P. B. Chilson, 2020: Confronting the boundary layer data gap: evaluating new and existing methodologies of probing the lower atmosphere. *Atmospheric Measurement Techniques*, **13 (7)**, 3855–3872.

Bell, T. M., P. M. Klein, J. K. Lundquist, and S. Waugh, 2021: Remote-sensing and radiosonde datasets collected in the san luis valley during the lapse-rate campaign. *Earth System Science Data*, **13 (3)**, 1041–1051.

Blackadar, A. K., 1957a: Boundary layer wind maxima and their significance for the growth of nocturnal inversions. *Bulletin of the American Meteorological Society*,

38 (5), 283–290, doi:10.1175/1520-0477-38.5.283, URL https://journals.ametsoc.org/view/journals/bams/38/5/1520-0477-38_5_283.xml, iSBN: 9781520047737 Publisher: American Meteorological Society Section: Bulletin of the American Meteorological Society.

Blackadar, A. K., 1957b: Boundary layer wind maxima and their significance for the growth of nocturnal inversions. *Bulletin of the American Meteorological Society*, **38 (5)**, 283–290.

Bonin, T., P. Chilson, B. Zielke, and E. Fedorovich, 2013: Observations of the early evening boundary-layer transition using a small unmanned aerial system. *Boundary-Layer Meteorology*, **146 (1)**, 119–132.

Bonner, W. D., 1966: Case study of thunderstorm activity in relation to the low-level jet. *Monthly Weather Review*, **94 (3)**, 167–178, doi:10.1175/1520-0493(1966)094⟨0167:CSOTAI⟩2.3.CO;2, URL https://journals.ametsoc.org/view/journals/mwre/94/3/1520-0493_1966_094_0167_csotai_2_3_co_2.xml, publisher: American Meteorological Society Section: Monthly Weather Review.

Bonner, W. D., 1968: Climatology of the low-level jet. *Monthly Weather Review*, **96 (12)**, 833–850, doi:10.1175/1520-0493(1968)096⟨0833:COTLLJ⟩2.0.CO;2, URL https://journals.ametsoc.org/view/journals/mwre/96/12/1520-0493_1968_096_0833_cotllj_2_0_co_2.xml, publisher: American Meteorological Society Section: Monthly Weather Review.

Browning, K. A., and Coauthors, 2007: The convective storm initiation project. *Bulletin of the American Meteorological Society*, **88 (12)**, 1939–1956.

Brus, D., J. Gustafsson, V. Vakkari, O. Kemppinen, G. de Boer, and A. Hirsikko, 2021: Measurement report: Properties of aerosol and gases in the vertical profile during the lapse-rate campaign. *Atmospheric Chemistry and Physics*, **21 (1)**, 517–533.

Calhoun, R., R. Heap, M. Princevac, R. Newsom, H. Fernando, and D. Ligon, 2006: Virtual towers using coherent doppler lidar during the joint urban 2003 dispersion experiment. *Journal of Applied Meteorology and Climatology*, **45 (8)**, 1116–1126, doi:10.1175/JAM2391.1, URL https://journals.ametsoc.org/view/journals/apme/45/8/jam2391.1.xml, publisher: American Meteorological Society Section: Journal of Applied Meteorology and Climatology.

Campbell, S., D. Clark, and J. Evans, 2017: Preliminary uas weather research roadmap. *Lincoln Laboratory, Massachusetts Institute of Technology*, **244**.

Cassano, J. J., 2014: Observations of atmospheric boundary layer temperature profiles with a small unmanned aerial vehicle. *Antarctic Science*, **26 (2)**, 205–213, doi:http://dx.doi.org/10.1017/S0954102013000539, URL https://www.proquest.com/docview/

1529781483/abstract/2DA94105885B49F7PQ/1, num Pages: 9 Place: Cambridge, United Kingdom Publisher: Cambridge University Press.

Chachere, C. N., and Z. Pu, 2016: Connections between cold air pools and mountain valley fog events in salt lake city. *Pure and Applied Geophysics*, **173 (9)**, 3187–3196.

Chan, P., 2008: Determination of richardson number profile from remote sensing data and its aviation application. *IOP Conference Series: Earth and Environmental Science*, IOP Publishing, Vol. 1, 012043.

Chan, S. T., and M. J. Leach, 2007: A validation of FEM3MP with Joint Urban 2003 data. *Journal of Applied Meteorology and Climatology*, **46 (12)**, 2127–2146, doi:10.1175/2006JAMC1321.1, URL https://journals.ametsoc.org/view/journals/apme/46/12/2006jamc1321.1.xml, publisher: American Meteorological Society Section: Journal of Applied Meteorology and Climatology.

Chen, J., S. Hagos, H. Xiao, J. D. Fast, and Z. Feng, 2020: Characterization of surface heterogeneity-induced convection using cluster analysis. *Journal of Geophysical Research: Atmospheres*, **125 (20)**, e2020JD032 550.

Chilson, P. B., and Coauthors, 2019: Moving towards a network of autonomous uas atmospheric profiling stations for observations in the earth's lower atmosphere: The 3d mesonet concept. *Sensors*, **19 (12)**, 2720.

Cione, J. J., E. A. Kalina, E. W. Uhlhorn, A. M. Farber, and B. Damiano, 2016: Coyote unmanned aircraft system observations in Hurricane Edouard (2014). *Earth and Space Science*, **3 (9)**, 370–380, doi:10.1002/2016EA000187, URL https://agupubs.onlinelibrary.wiley.com/doi/abs/10.1002/2016EA000187, _eprint: https://agupubs.onlinelibrary.wiley.com/doi/pdf/10.1002/2016EA000187.

Coniglio, M. C., G. S. Romine, D. D. Turner, and R. D. Torn, 2019: Impacts of targeted aeri and doppler lidar wind retrievals on short-term forecasts of the initiation and early evolution of thunderstorms. *Monthly Weather Review*, **147 (4)**, 1149–1170.

Dai, C., Q. Wang, J. Kalogiros, D. Lenschow, Z. Gao, and M. Zhou, 2014: Determining boundary-layer height from aircraft measurements. *Boundary-Layer Meteorology*, **152 (3)**, 277–302.

Dang, R., Y. Yang, X.-M. Hu, Z. Wang, and S. Zhang, 2019: A review of techniques for diagnosing the atmospheric boundary layer height (ablh) using aerosol lidar data. *Remote Sensing*, **11 (13)**, 1590.

de Boer, G., and Coauthors, 2020a: Data generated during the 2018 lapse-rate campaign: an introduction and overview. *Earth System Science Data*, **12 (4)**, 3357–3366.

de Boer, G., and Coauthors, 2020b: Development of community, capabilities, and understanding through unmanned aircraft-based atmospheric research: The lapse-rate campaign. *Bulletin of the American Meteorological Society*, **101 (5)**, E684–E699.

Deardorff, J., G. Willis, and B. Stockton, 1980: Laboratory studies of the entrainment zone of a convectively mixed layer. *Journal of Fluid Mechanics*, **100 (1)**, 41–64.

Desmond, K., 2018: *Electric airplanes and drones: A history.* McFarland, 171-174 pp.

Elston, J., B. Argrow, M. Stachura, D. Weibel, D. Lawrence, and D. Pope, 2015: Overview of small fixed-wing unmanned aircraft for meteorological sampling. *Journal of Atmospheric and Oceanic Technology*, **32 (1)**, 97–115.

Elston, J. S., J. Roadman, M. Stachura, B. Argrow, A. Houston, and E. Frew, 2011: The tempest unmanned aircraft system for in situ observations of tornadic supercells: Design and VORTEX2 flight results. *Journal of Field Robotics*, **28 (4)**, 461–483, doi: 10.1002/rob.20394, URL http://doi.wiley.com/10.1002/rob.20394.

Emmanuel, C., 1973: Richardson number profiles through shear instability wave regions observed in the lower planetary boundary layer. *Boundary-Layer Meteorology*, **5 (1)**, 19–27.

Fedorovich, E., J. A. Gibbs, and A. Shapiro, 2017: Numerical study of nocturnal low-level jets over gently sloping terrain. *Journal of the Atmospheric Sciences*, **74 (9)**, 2813–2834, doi:10.1175/JAS-D-17-0013.1, URL https://journals.ametsoc.org/view/journals/atsc/74/9/jas-d-17-0013.1.xml, publisher: American Meteorological Society Section: Journal of the Atmospheric Sciences.

Flagg, D. D., and Coauthors, 2018: On the impact of unmanned aerial system observations on numerical weather prediction in the coastal zone. *Monthly Weather Review*, **146 (2)**, 599–622, doi:10.1175/MWR-D-17-0028.1, URL https://journals.ametsoc.org/view/journals/mwre/146/2/mwr-d-17-0028.1.xml, publisher: American Meteorological Society Section: Monthly Weather Review.

Frew, E. W., B. Argrow, S. Borenstein, S. Swenson, C. A. Hirst, H. Havenga, and A. Houston, 2020: Field observation of tornadic supercells by multiple autonomous fixed-wing unmanned aircraft. *Journal of Field Robotics*, **37 (6)**, 1077–1093, doi:10.1002/rob.21947, URL https://onlinelibrary.wiley.com/doi/abs/10.1002/rob.21947, _eprint: https://onlinelibrary.wiley.com/doi/pdf/10.1002/rob.21947.

Frye, J. D., and T. L. Mote, 2010: Convection initiation along soil moisture boundaries in the southern great plains. *Monthly Weather Review*, **138 (4)**, 1140–1151.

Gebauer, J. G., E. Fedorovich, and A. Shapiro, 2017: A 1d theoretical analysis of northerly low-level jets over the great plains. *Journal of the Atmospheric Sciences*, **74 (10)**, 3419–3431.

Greene, B. R., A. R. Segales, T. M. Bell, E. A. Pillar-Little, and P. B. Chilson, 2019: Environmental and sensor integration influences on temperature measurements by rotary-wing unmanned aircraft systems. *Sensors*, **19 (6)**, 1470.

Greene, B. R., A. R. Segales, S. Waugh, S. Duthoit, and P. B. Chilson, 2018: Considerations for temperature sensor placement on rotary-wing unmanned aircraft systems. *Atmospheric Measurement Techniques*, **11 (10)**, 5519.

Hennemuth, B., and A. Lammert, 2006: Determination of the atmospheric boundary layer height from radiosonde and lidar backscatter. *Boundary-Layer Meteorology*, **120 (1)**, 181–200.

Herdies, D. L., V. E. Kousky, and W. Ebisuzaki, 2007: The Impact of High-Resolution SALLJEX Data on Global NCEP Analyses. *Journal of Climate*, **20 (23)**, 5765–5783, doi:10.1175/2007JCLI1375.1, URL https://journals.ametsoc.org/view/journals/clim/20/23/2007jcli1375.1.xml, publisher: American Meteorological Society Section: Journal of Climate.

Higgins, R. W., Y. Yao, E. S. Yarosh, J. E. Janowiak, and K. C. Mo, 1997: Influence of the Great Plains low-level jet on summertime precipitation and moisture transport over the central United States. *Journal of Climate*, **10 (3)**, 481–507, doi:10.1175/1520-0442(1997)010⟨0481:IOTGPL⟩2.0.CO;2, URL https://journals.ametsoc.org/view/journals/clim/10/3/1520-0442_1997_010_0481_iotgpl_2.0.co_2.xml, publisher: American Meteorological Society Section: Journal of Climate.

Holton, J. R., 1967: The diurnal boundary layer wind oscillation above sloping terrain. *Tellus*, **19 (2)**, 200–205, doi:10.3402/tellusa.v19i2.9766, URL https://doi.org/10.3402/tellusa.v19i2.9766, publisher: Taylor & Francis _eprint: https://doi.org/10.3402/tellusa.v19i2.9766.

Houston, A. L., and D. Niyogi, 2007: The sensitivity of convective initiation to the lapse rate of the active cloud-bearing layer. *Monthly Weather Review*, **135 (9)**, 3013–3032.

Hu, J., N. Yussouf, D. D. Turner, T. A. Jones, and X. Wang, 2019: Impact of ground-based remote sensing boundary layer observations on short-term probabilistic forecasts of a tornadic supercell event. *Weather and Forecasting*, **34 (5)**, 1453–1476.

Hu, X.-M., P. M. Klein, M. Xue, F. Zhang, D. C. Doughty, R. Forkel, E. Joseph, and J. D. Fuentes, 2013: Impact of the vertical mixing induced by low-level jets on boundary layer ozone concentration. *Atmospheric Environment*, **70**, 123–130, doi:10.1016/j.atmosenv.2012.12.046, URL https://www.sciencedirect.com/science/article/pii/S135223101300023X.

Jacob, J. D., P. B. Chilson, A. L. Houston, and S. W. Smith, 2018: Considerations for Atmospheric Measurements with Small Unmanned Aircraft Systems. *Atmosphere*,

9 (7), 252, doi:10.3390/atmos9070252, URL https://www.mdpi.com/2073-4433/9/7/252, number: 7 Publisher: Multidisciplinary Digital Publishing Institute.

Jensen, A. A., and Coauthors, 2021: Assimilation of a Coordinated Fleet of Uncrewed Aircraft System Observations in Complex Terrain: EnKF System Design and Preliminary Assessment. *Monthly Weather Review*, **149 (5)**, 1459–1480, doi:10.1175/MWR-D-20-0359.1, URL https://journals.ametsoc.org/view/journals/mwre/149/5/MWR-D-20-0359.1.xml, publisher: American Meteorological Society Section: Monthly Weather Review.

Jonassen, M. O., H. Ólafsson, H. Ágústsson, Ó. Rögnvaldsson, and J. Reuder, 2012: Improving high-resolution numerical weather simulations by assimilating data from an unmanned aerial system. *Monthly Weather Review*, **140 (11)**, 3734–3756.

Jonassen, M. O., P. Tisler, B. Altstädter, A. Scholtz, T. Vihma, A. Lampert, G. König-Langlo, and C. Lüpkes, 2015: Application of remotely piloted aircraft systems in observing the atmospheric boundary layer over antarctic sea ice in winter. *Polar Research*, **34 (1)**, 25 651.

Kang, S.-L., and G. H. Bryan, 2011: A large-eddy simulation study of moist convection initiation over heterogeneous surface fluxes. *Monthly weather review*, **139 (9)**, 2901–2917.

Koch, S. E., M. Fengler, P. B. Chilson, K. L. Elmore, B. Argrow, D. L. Andra Jr, and T. Lindley, 2018: On the use of unmanned aircraft for sampling mesoscale phenomena in the preconvective boundary layer. *Journal of Atmospheric and Oceanic Technology*, **35 (11)**, 2265–2288.

Kondo, J., O. Kanechika, and N. Yasuda, 1978: Heat and momentum transfers under strong stability in the atmospheric surface layer. *Journal of Atmospheric Sciences*, **35 (6)**, 1012–1021.

Kral, S. T., and Coauthors, 2018: Innovative strategies for observations in the arctic atmospheric boundary layer (ISOBAR)—the hailuoto 2017 campaign. *Atmosphere*, **9 (7)**, 268.

Krishnamurthy, R., R. Calhoun, B. Billings, and J. Doyle, 2011: Wind turbulence estimates in a valley by coherent Doppler lidar. *Meteorological Applications*, **18 (3)**, 361–371, doi:10.1002/met.263, URL https://rmets.onlinelibrary.wiley.com/doi/abs/10.1002/met.263, _eprint: https://rmets.onlinelibrary.wiley.com/doi/pdf/10.1002/met.263.

Lenschow, D., B. Stankov, and L. Mahrt, 1979: The rapid morning boundary-layer transition. *Journal of the Atmospheric Sciences*, **36 (11)**, 2108–2124.

Lettau, H. H., and B. Davidson, 1957: *Exploring the atmosphere's first mile : proceedings of the Great Plains turbulence field program 1 August to 8 September 1953, O'Neill, Nebraska.* Pergamon London, 2v. [v.p.] : pp.

Lewis, W. E., T. J. Wagner, J. A. Otkin, and T. A. Jones, 2020: Impact of aeri temperature and moisture retrievals on the simulation of a central plains severe convective weather event. *Atmosphere*, **11 (7)**, 729.

Li, Z., and Coauthors, 2017: Aerosol and boundary-layer interactions and impact on air quality. *National Science Review*, **4 (6)**, 810–833, doi:10.1093/nsr/nwx117, URL https://doi.org/10.1093/nsr/nwx117.

Lundby, T., M. P. Christiansen, and K. Jensen, 2019: Towards a Weather Analysis Software Framework to Improve UAS Operational Safety. *2019 International Conference on Unmanned Aircraft Systems (ICUAS)*, 1372–1380, doi:10.1109/ICUAS.2019.8798271, iSSN: 2575-7296.

Maddox, R. A., 1983: Large-scale meteorological conditions associated with midlatitude, mesoscale convective complexes. *Monthly Weather Review*, **111 (7)**, 1475–1493.

Martucci, G., R. Matthey, V. Mitev, and H. Richner, 2007: Comparison between backscatter lidar and radiosonde measurements of the diurnal and nocturnal stratification in the lower troposphere. *Journal of Atmospheric and Oceanic Technology*, **24 (7)**, 1231–1244.

Mayer, S., A. Sandvik, M. O. Jonassen, and J. Reuder, 2012: Atmospheric profiling with the uas sumo: a new perspective for the evaluation of fine-scale atmospheric models. *Meteorology and Atmospheric Physics*, **116 (1)**, 15–26.

Mccorcle, M. D., 1988: Simulation of surface-moisture effects on the great plains low-level jet. *Monthly Weather Review*, **116 (9)**, 1705–1720.

Mirocha, J. D., M. D. Simpson, J. D. Fast, L. K. Berg, and R. Baskett, 2016: Investigation of boundary-layer wind predictions during nocturnal low-level jet events using the weather research and forecasting model. *Wind Energy*, **19 (4)**, 739–762.

Mohan, M., and T. Siddiqui, 1998: Analysis of various schemes for the estimation of atmospheric stability classification. *Atmospheric Environment*, **32 (21)**, 3775–3781.

Monti, P., H. J. S. Fernando, M. Princevac, W. C. Chan, T. A. Kowalewski, and E. R. Pardyjak, 2002: Observations of flow and turbulence in the nocturnal boundary layer over a slope. *Journal of the Atmospheric Sciences*, **59 (17)**, 2513–2534, doi:10.1175/1520-0469(2002)059⟨2513:OOFATI⟩2.0.CO;2, URL https://journals.ametsoc.org/view/journals/atsc/59/17/1520-0469_2002_059_2513_oofati_2.0.co_2.xml, publisher: American Meteorological Society Section: Journal of the Atmospheric Sciences.

National Research Council, 2009: *Observing weather and climate from the ground up: A nationwide network of networks*. National Academies Press.

Ohya, Y., R. Nakamura, and T. Uchida, 2008: Intermittent bursting of turbulence in a stable boundary layer with low-level jet. *Boundary-layer meteorology*, **126 (3)**, 349–363.

Ohya, Y., D. E. Neff, and R. N. Meroney, 1997: Turbulence structure in a stratified boundary layer under stable conditions. *Boundary-Layer Meteorology*, **83 (1)**, 139–162.

Pal, S., T. R. Lee, S. Phelps, and S. F. J. De Wekker, 2014: Impact of atmospheric boundary layer depth variability and wind reversal on the diurnal variability of aerosol concentration at a valley site. *The Science of the Total Environment*, **496**, 424–434, doi:10.1016/j.scitotenv.2014.07.067.

Pillar-Little, E. A., and Coauthors, 2021: Observations of the thermodynamic and kinematic state of the atmospheric boundary layer over the san luis valley, co, using the coptersonde 2 remotely piloted aircraft system in support of the lapse-rate field campaign. *Earth System Science Data*, **13 (2)**, 269–280.

Pinto, J. O., A. A. Jensen, P. A. Jiménez, T. Hertneky, D. Muñoz-Esparza, A. Dumont, and M. Steiner, 2021: Real-time WRF large-eddy simulations to support uncrewed aircraft system (UAS) flight planning and operations during 2018 LAPSE-RATE. *Earth System Science Data*, **13 (2)**, 697–711, doi:10.5194/essd-13-697-2021, URL https://essd.copernicus.org/articles/13/697/2021/, publisher: Copernicus GmbH.

Poulos, G. S., and S. P. Burns, 2003: An evaluation of bulk ri-based surface layer flux formulas for stable and very stable conditions with intermittent turbulence. *Journal of the atmospheric sciences*, **60 (20)**, 2523–2537.

Ranquist, E., M. Steiner, and B. Argrow, 2017: Exploring the range of weather impacts on UAS operations. AMS, URL https://ams.confex.com/ams/97Annual/webprogram/Paper309274.html.

Rasmussen, E., 2015: Vortex-southeast program overview. *National Severe Storms Laboratory Rep*, **36**.

Reeves, H. D., 2016: The uncertainty of precipitation-type observations and its effect on the validation of forecast precipitation type. *Weather and Forecasting*, **31 (6)**, 1961–1971.

Reuder, J., P. Brisset, M. Jonassen, M. Müller, and S. Mayer, 2009: The small unmanned meteorological observer sumo: A new tool for atmospheric boundary layer research. *Meteorologische Zeitschrift*, **18 (2)**, 141–147.

Rochetin, N., F. Couvreux, and F. Guichard, 2017: Morphology of breeze circulations induced by surface flux heterogeneities and their impact on convection initiation. *Quarterly Journal of the Royal Meteorological Society*, **143 (702)**, 463–478.

Rohr, J., E. Itsweire, K. Helland, and C. Van Atta, 1988: Growth and decay of turbulence in a stably stratified shear flow. *Journal of Fluid Mechanics*, **195**, 77–111.

Roseman, C. A., and B. M. Argrow, 2020: Weather hazard risk quantification for sUAS safety risk management. *Journal of Atmospheric and Oceanic Technology*, **37 (7)**, 1251–1268, doi:10.1175/JTECH-D-20-0009.1, URL https://journals. ametsoc.org/view/journals/atot/37/7/jtechD200009.xml, publisher: American Meteorological Society Section: Journal of Atmospheric and Oceanic Technology.

Roseman, C. A., and J. O. Pinto, 2019: Targeted weather forecasts for small unmanned aircraft systems. AMS, URL https://ams.confex.com/ams/2019Annual/ webprogram/Paper351492.html.

Ryu, Y.-H., J. A. Smith, E. Bou-Zeid, and M. L. Baeck, 2016: The influence of land surface heterogeneities on heavy convective rainfall in the baltimore–washington metropolitan area. *Monthly Weather Review*, **144 (2)**, 553–573.

Segales, A. R., B. R. Greene, T. M. Bell, W. Doyle, J. J. Martin, E. A. Pillar-Little, and P. B. Chilson, 2020: The coptersonde: an insight into the development of a smart unmanned aircraft system for atmospheric boundary layer research. *Atmospheric Measurement Techniques*, **13 (5)**.

Shapiro, A., and E. Fedorovich, 2009: Nocturnal low-level jet over a shallow slope. *Acta Geophysica*, **57 (4)**, 950–980.

Shapiro, A., E. Fedorovich, and S. Rahimi, 2016: A unified theory for the great plains nocturnal low-level jet. *Journal of the Atmospheric Sciences*, **73 (8)**, 3037–3057.

Silcox, G. D., K. E. Kelly, E. T. Crosman, C. D. Whiteman, and B. L. Allen, 2012: Wintertime PM2.5 concentrations during persistent, multi-day cold-air pools in a mountain valley. *Atmospheric Environment*, **46**, 17–24, doi:10.1016/j.atmosenv.2011.10. 041, URL https://www.sciencedirect.com/science/article/pii/S1352231011011204.

Skabar, Y. G., and M. Nicolini, 2009: Enriched analyses with assimilation of SALLJEX data. *Journal of Applied Meteorology and Climatology*, **48 (12)**, 2425–2440, doi:10.1175/2009JAMC2091.1, URL https://journals.ametsoc.org/view/ journals/apme/48/12/2009jamc2091.1.xml, publisher: American Meteorological Society Section: Journal of Applied Meteorology and Climatology.

Smith, E. N., J. G. Gebauer, P. M. Klein, E. Fedorovich, and J. A. Gibbs, 2019: The great plains low-level jet during pecan: Observed and simulated characteristics. *Monthly Weather Review*, **147 (6)**, 1845–1869.

Squitieri, B. J., and W. A. Gallus, 2016: WRF forecasts of Great Plains nocturnal low-level jet-driven MCSs. Part I: Correlation between low-level jet forecast accuracy and MCS precipitation forecast skill. *Weather and Forecasting*, **31 (4)**, 1301–1323, doi: 10.1175/WAF-D-15-0151.1, URL https://journals.ametsoc.org/view/journals/wefo/ 31/4/waf-d-15-0151_1.xml, publisher: American Meteorological Society Section: Weather and Forecasting.

Stensrud, D. J., 1996: Importance of low-level jets to climate: A review. *Journal of Climate*, **9 (8)**, 1698–1711, doi:10.1175/1520-0442(1996)009⟨1698:IOLLJT⟩2.0. CO;2, URL https://journals.ametsoc.org/view/journals/clim/9/8/1520-0442_1996_ 009_1698_iolljt_2_0_co_2.xml, publisher: American Meteorological Society Section: Journal of Climate.

Storm, B., J. Dudhia, S. Basu, A. Swift, and I. Giammanco, 2009: Evaluation of the Weather Research and Forecasting model on forecasting low-level jets: implications for wind energy. *Wind Energy*, **12 (1)**, 81–90, doi:10. 1002/we.288, URL https://onlinelibrary.wiley.com/doi/abs/10.1002/we.288, _eprint: https://onlinelibrary.wiley.com/doi/pdf/10.1002/we.288.

Stull, R., 1988: 1988: An introduction to boundary layer meteorology. *K luwer A cademic Publishers*.

Sullivan, J. T., S. D. Rabenhorst, J. Dreessen, T. J. McGee, R. Delgado, L. Twigg, and G. Sumnicht, 2017: Lidar observations revealing transport of O3 in the presence of a nocturnal low-level jet: Regional implications for "next-day" pollution. *Atmospheric Environment*, **158**, 160–171, doi:10.1016/j.atmosenv.2017.03.039, URL https://www.sciencedirect.com/science/article/pii/S1352231017301711.

Sun, J., L. Mahrt, R. M. Banta, and Y. L. Pichugina, 2012: Turbulence regimes and turbulence intermittency in the stable boundary layer during cases-99. *Journal of Atmospheric Sciences*, **69 (1)**, 338–351.

Sun, J., and Coauthors, 2015: Review of wave-turbulence interactions in the stable atmospheric boundary layer. *Reviews of Geophysics*, **53 (3)**, 956–993, doi:10.1002/2015RG000487, URL https: //agupubs.onlinelibrary.wiley.com/doi/abs/10.1002/2015RG000487, _eprint: https://agupubs.onlinelibrary.wiley.com/doi/pdf/10.1002/2015RG000487.

Trier, S. B., C. A. Davis, D. A. Ahijevych, and K. W. Manning, 2014: Use of the parcel buoyancy minimum (b min) to diagnose simulated thermodynamic destabilization. part i: Methodology and case studies of mcs initiation environments. *Monthly Weather Review*, **142 (3)**, 945–966.

Trier, S. B., and D. B. Parsons, 1993: Evolution of environmental conditions preceding the development of a nocturnal mesoscale convective complex. *Monthly weather review*, **121 (4)**, 1078–1098.

Tripp, D. D., E. R. Martin, and H. D. Reeves, 2021: Applications of uncrewed aerial vehicles (uavs) in winter precipitation-type forecasts. *Journal of Applied Meteorology and Climatology*, **60 (3)**, 361–375.

Villa, T. F., F. Gonzalez, B. Miljievic, Z. D. Ristovski, and L. Morawska, 2016: An overview of small unmanned aerial vehicles for air quality measurements: Present applications and future prospectives. *Sensors*, **16 (7)**, 1072.

Vogelezang, D. H. P., and A. A. M. Holtslag, 1996: Evaluation and model impacts of alternative boundary-layer height formulations. *Boundary-Layer Meteorology*, **81 (3)**, 245–269, doi:10.1007/BF02430331, URL https://doi.org/10.1007/BF02430331.

Wagner, T. J., P. M. Klein, and D. D. Turner, 2019: A new generation of ground-based mobile platforms for active and passive profiling of the boundary layer. *Bulletin of the American Meteorological Society*, **100 (1)**, 137–153.

Weckwerth, T. M., T. W. Horst, and J. W. Wilson, 1999: An observational study of the evolution of horizontal convective rolls. *Monthly Weather Review*, **127 (9)**, 2160–2179.

Weisman, M. L., and R. Rotunno, 2004: "A theory for strong long-lived squall lines" revisited. *Journal of the Atmospheric Sciences*, **61 (4)**, 361–382.

Whiteman, C. D., and T. B. McKee, 1978: Air pollution implications of inversion descent in mountain valleys. *Atmospheric Environment (1967)*, **12 (11)**, 2151–2158, doi:10.1016/0004-6981(78)90170-1, URL https://www.sciencedirect.com/science/article/pii/0004698178901701.

Wildmann, N., N. Bodini, J. K. Lundquist, L. Bariteau, and J. Wagner, 2019: Estimation of turbulence dissipation rate from Doppler wind lidars and in situ instrumentation for the Perdigão 2017 campaign. *Atmospheric Measurement Techniques*, **12 (12)**, 6401–6423, doi:10.5194/amt-12-6401-2019, URL https://amt.copernicus.org/articles/12/6401/2019/, publisher: Copernicus GmbH.

Zhang, Y., and S. A. Klein, 2010: Mechanisms affecting the transition from shallow to deep convection over land: Inferences from observations of the diurnal cycle collected at the arm southern great plains site. *Journal of the Atmospheric Sciences*, **67 (9)**, 2943–2959.

Ziegler, C. L., and E. N. Rasmussen, 1998: The initiation of moist convection at the dryline: forecasting issues from acase study perspective. *Weather and Forecasting*, **13 (4)**, 1106–1131.

Ágústsson, H., H. Ólafsson, M. O. Jonassen, and Rögnvaldsson, 2014: The impact of assimilating data from a remotely piloted aircraft on simulations of weak-wind orographic flow. *Tellus A: Dynamic Meteorology and Oceanography*, **66 (1)**, 25 421,

doi:10.3402/tellusa.v66.25421, URL https://doi.org/10.3402/tellusa.v66.25421, publisher: Taylor & Francis _eprint: https://doi.org/10.3402/tellusa.v66.25421.

1 Appendix A

In order to deliver a salient comparison of Ri profiles from two datasets, it requires as few independent variables as possible. Since radiosondes have an innate confidence in measurements, the CopterSonde data must be adjusted to match. Much effort went into assimilating the CopterSonde data to the level of the radiosonde data. While the methods of smoothing on radiosonde winds are uncertain, it is empirically decided that the wind data have a 150 m boxcar mean applied. Since the CopterSonde has altitude restraints, the data cannot afford to be smoothed to that extent. Nevertheless, to complete a cross-comparison between Coptersonde and radiosonde it is necessary that the data behave as similarly as possible. The remainder of this section will describe the various techniques and reasoning behind the final smoothing technique.

Methods from a few studies such as Balsley et al. (2006) and Dai et al. (2014) are applied but no one method does an adequate job. Polynomial and sliding linear fittings, similar to methods from Balsley et al. (2006), give consecutive profiles that are largely different. The standard deviation of temporally averaged profiles over a 2 h span illustrates the wide spread (Fig. A.1). Also, the mode of the Ri profile is on the order of 10 which is much higher than expected in a nearly neutral environment. The time span of 2236-0035 UTC is chosen because the profile heights are consistent and the CBL is vertically homogeneous. Also, the raw comparison showed large discrepancies between the data. If a method improved the largest errors, it is assumed it would also benefit times with smaller errors. Dai et al. (2014) approximates Ri using the Rb through smoothing then finite differencing. A few issues arose from finite differencing, with or without prior smoothing. Rb becomes highly dependent on layer depth, which also dictates the data resolution. For the most part, the larger the layer depth the smaller the Ri (Fig. A.2). Using the 20 m depth to replicate Dai et al. (2014), Ri values are roughly a magnitude smaller than typical values. The shallow layer depth and large wind shear undervalue Ri. Running means act as a low pass filter, leaving profiles with better resemblance to those from radiosondes. Additionally, a running mean applied to the gradients scaled the magnitude of fluctuations down considerably. While running means were beneficial to reducing the standard deviation throughout a profile, there is still a strong dependence on the running mean length.

The CopterSonde collects kinematic and thermodynamic variables differently, so logically the running mean lengths are not the same. Since wind speed and direction are not directly sensed, rather backed out using Windvane mode (Segales et al., 2020) there is more random error. As a result, wind components need a longer running mean than potential temperature. Similar to radiosonde data, the potential temperature data converge to a common profile past a running mean length of about 20 m. This is not the case for the kinematic data. There is a fine line between reducing the RMSE between the two datasets and the profile just smoothing to small values, thus decreasing RMSE. Since Ri is composed of two vertical gradients, it aided in comparison to dissect each and compare across datasets in addition to the final Ri profile. The Brunt-Väisälä squared term becomes comparable with a shorter rolling average (Fig. A.3,

A.4). There was an inverse correlation with the RMSE and running mean length, but comparing the profiles, the RMSE only goes down because the CopterSonde's *Ri* values are much smaller. Even though the wind shear profiles look more similar with the longer running mean length, the RMSE is barely impacted (Fig. A.3, A.5). The additional running mean applied to the gradients negatively impact the RMSE but makes their appearances more alike. The fluctuation frequency and intensity are reduced, yet the RMSE is nearly six times higher (Fig. A.6, A.5). So it appears, a point-by-point statistical comparison does not offer a complete description. Perhaps the nonlinearity is impacting the statistics. For all of the arguments made, this is the best solution for the time being.

Ultimately, the smoothing technique became a subjective decision to prioritize similarity in appearance over the reduction of RMSE. Figure 3.4 illustrates the best representation found. The standard deviations are within a magnitude of the mean. The fluctuations from each dataset are comparable, especially after 2029 UTC. Until a better statistical approach is found to quantify differences the final technique follows: applied running means are 100 m on the U and V wind components, 20 m on potential temperature, and 5 m on each gradient.
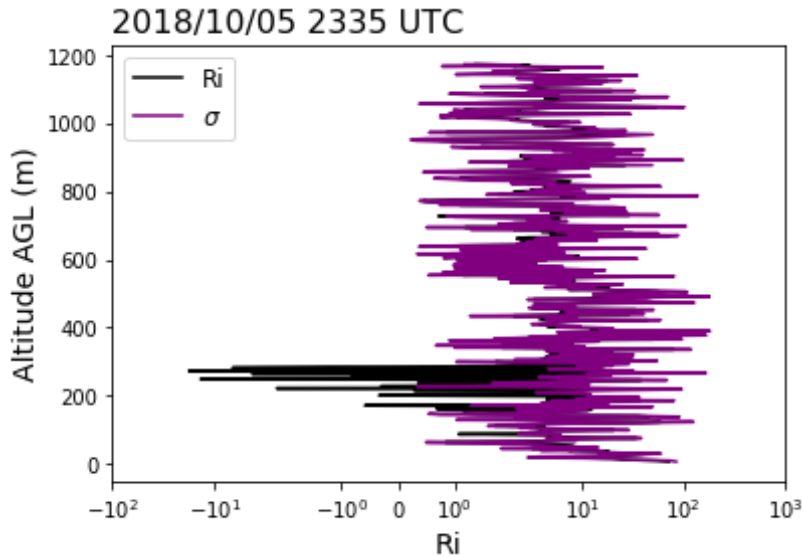

Figure A.1: Ri (black) and its standard deviation (purple) calculated using polynomial fitting at 2335 UTC 05 October 2018.
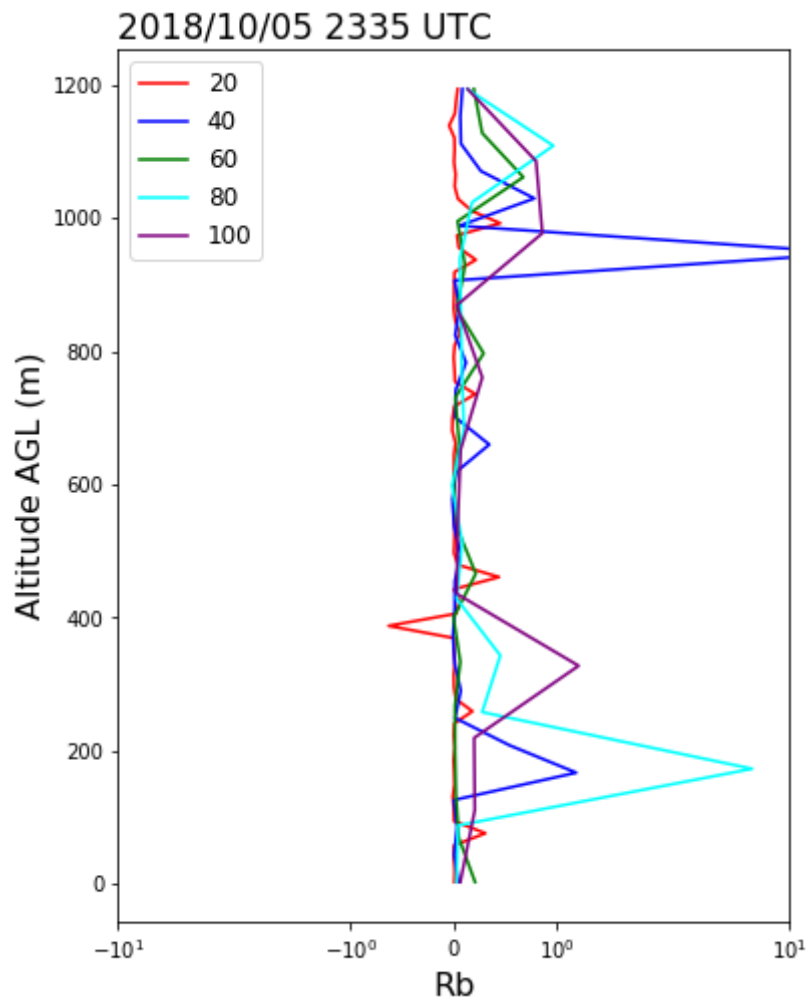
Figure A.2: Ri with height calculated using finite differencing at various depths (m) at 2335 UTC 05 October 2018
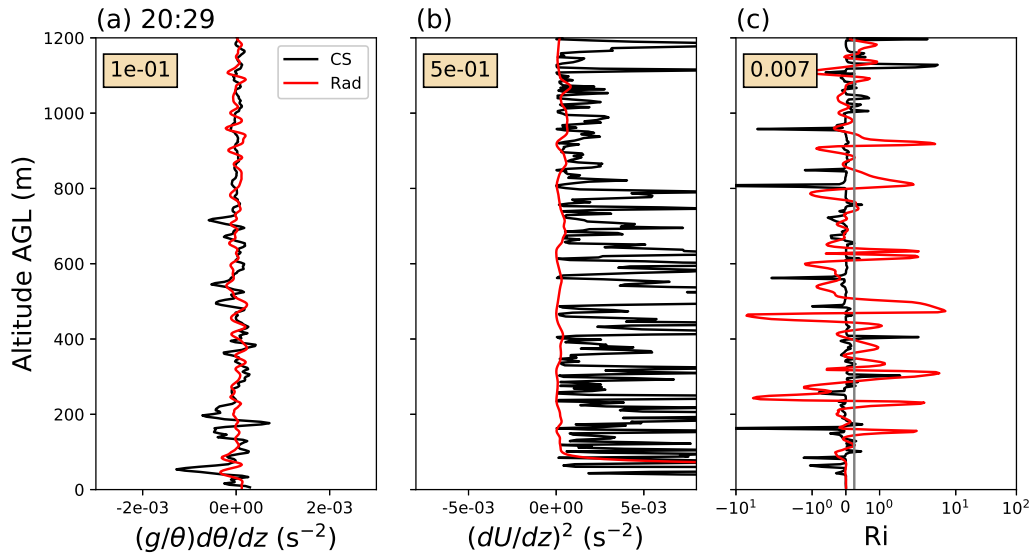
Figure A.3: Ri and its components on 2029 UTC 05 October 2018 from CopterSonde (black) and radiosonde (red) data. (a) Brunt-Väisälä squared term with 20 m running mean applied to CopterSonde potential temperature (s^{-2}). (b) Squared vertical wind shear with 40 m running mean applied to CopterSonde wind components (s^{-2}). (c) Ri with height. The tan boxes indicate the RMSE between the CopterSonde and radiosonde values.
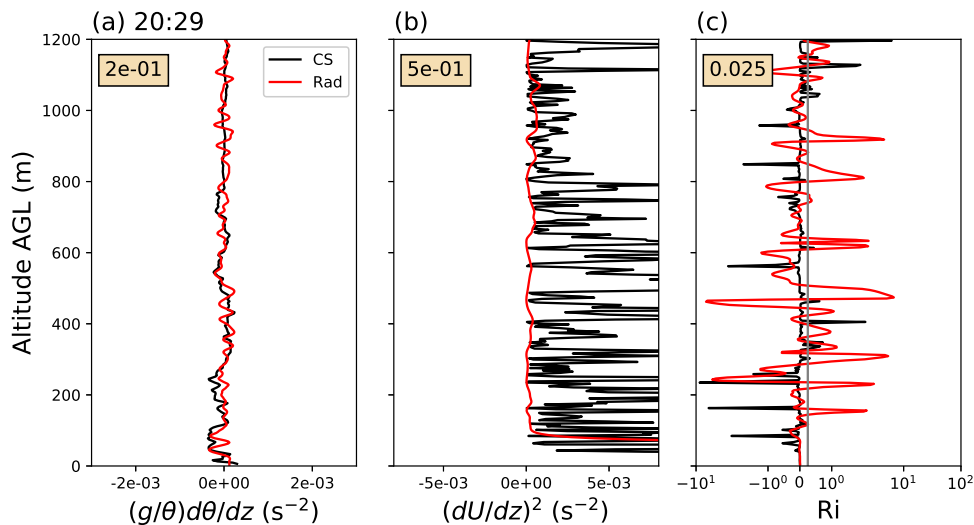

Figure A.4: Same as Fig. A.3 but the Brunt-Väisälä squared term had a 60 m running mean applied to potential temperature prior to calculation.
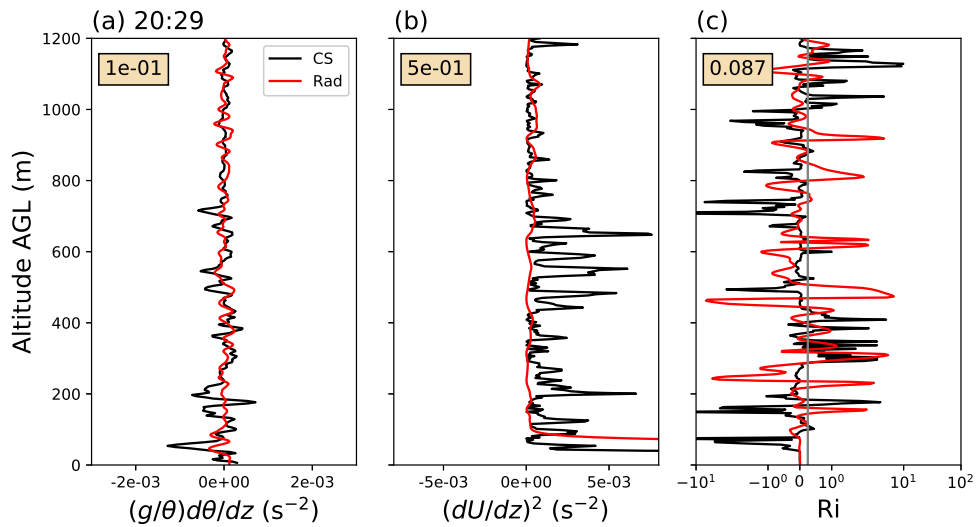
Figure A.5: Same as Fig. A.3 but the squared vertical wind shear term had a 100 m running mean applied to the wind components prior to calculation.
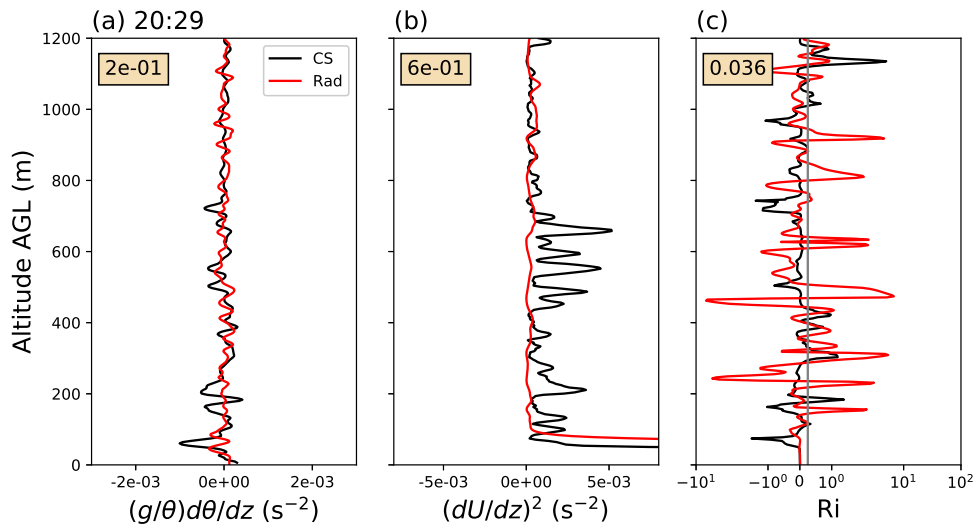

Figure A.6: Same as Fig. A.5 but an additional 5 m runnning mean was applied to the vertical potential gradient and vertical wind shear.